J. Fluid Mech. (1992), *vol.* 237, *pp.* 261–299
Printed in Great Britain

Numerical simulation of turbulent convection over wavy terrain

By KILIAN KRETTENAUER AND ULRICH SCHUMANN
DLR, Institute of Atmospheric Physics, W-8031 Oberpfaffenhofen, Germany

(Received 20 January 1991 and in revised form 17 September 1991)

Thermal convection of a Boussinesq fluid in a layer confined between two infinite horizontal walls is investigated by direct numerical simulation (DNS) and by large-eddy simulation (LES) for zero horizontal mean motion. The lower-surface height varies sinusoidally in one horizontal direction while remaining constant in the other. Several cases are considered with amplitude δ up to $0.15H$ and wavelength λ of H to $8H$ (inclination up to 43°), where H is the mean fluid-layer height. Constant heat flux is prescribed at the lower surface of the initially at rest and isothermal fluid layer. In the LES, the surface is treated as rough surface ($z_0 = 10^{-4}H$) using the Monin–Oboukhov relationships. At the flat top an adiabatic frictionless boundary condition is applied which approximates a strong capping inversion of an atmospheric convective boundary layer. In both horizontal directions, the model domain extends over the same length (either $4H$ or $8H$) with periodic lateral boundary conditions.

We compare DNS of moderate turbulence (Reynolds number based on H and on the convective velocity is 100, Prandtl number is 0.7) with LES of the fully developed turbulent state in terms of turbulence statistics and characteristic large-scale-motion structures. The LES results for a flat surface generally agree well with the measurements of Adrian *et al.* (1986). The gross features of the flow statistics, such as profiles of turbulence variances and fluxes, are found to be not very sensitive to the variations of wavelength, amplitude, domain size and resolution and even the model type (DNS or LES), whereas details of the flow structure are changed considerably. The LES shows more turbulent structures and larger horizontal scales than the DNS. To a weak degree, the orography enforces rolls with axes both perpendicular and parallel to the wave crests and with horizontal wavelengths of about $2H$ to $4H$. The orography has the largest effect for $\lambda = 4H$ in the LES and for $\lambda = 2H$ in the DNS. The results change little when the size of the computational domain is doubled in both horizontal directions. Most of the motion energy is contained in the large-scale structures and these structures are persistent in time over periods of several convective time units. The motion structure persists considerably longer over wavy terrain than over flat surfaces.

1. Introduction

Much is known about thermal convection over ideally homogeneous horizontal surfaces (Busse 1978; Stull 1988). Land surfaces are, however, rarely homogeneous. They are undulate and form hilly terrain. Even when the amplitude of the hilly terrain stays below the mean height of the atmospheric boundary layer, one might expect that the topography influences the flow structure considerably. In this paper, we investigate the effect of terrain on turbulent convection within a boundary layer

of finite depth over a wavy surface with constant surface heat flux and with zero mean horizontal motion. In order to identify the effects of wavy terrain as clearly as possible, we limit this study to surfaces with height varying sinusoidally in one direction only.

In the atmosphere, a convective boundary layer (CBL) forms between the surface and an inversion which is topped by stably stratified air (Stull 1988). The properties of such a 'penetrating' CBL depend at least weakly on the strength of the inversion and the stability of the layer above the turbulent CBL. Moreover, turbulence in the CBL is only quasi-steady because of growing boundary-layer depth. In this study, we consider a non-penetrating boundary layer capped by an adiabatic free-slip rigid wall. Such a boundary condition has intrinsic interest, but it also approximates the properties of a very strong temperature inversion above the CBL. For constant surface heat flux such a layer approaches a state in which all statistics of motions approach a strictly steady state. Only the mean temperature continues to increase linearly with time but this does not affect the flow which is driven solely by temperature differences. Hence, the parameter space for this problem is smaller than for the CBL and this property is attractive because of the additional parameters which enter the problem due to the wavy surface.

In a previous paper (Krettenauer & Schumann 1989*b*), we investigated the present problem for various finite Reynolds or Rayleigh numbers using direct numerical simulation (DNS). We found that the flow is turbulent for Reynolds numbers which are of the order ten times the critical one for the onset of laminar convection over flat surfaces. The results exhibited little sensitivity of the convection to the wavy surface for a 10% amplitude. However, the simulations were limited in the domain size and the wavelength; the domain contained only one surface wave and the wavelength was fixed ($\lambda = 2H$, where H is the mean fluid-layer height). We will show that more random structures arise for larger domain sizes. Moreover, our main objective is to describe the flow structure at very high Reynolds number, typical for atmospheric cases. For this purpose, we extend the method to include large-eddy simulation (LES). Such a simulation is designed to describe approximately the properties at the large scales that would be valid for infinite Reynolds number; see Nieuwstadt (1990) for a review of LES methods.

Relatively little is known about the impact of heterogeneity of the bounding surfaces. The case of periodic horizontal disturbances has been investigated analytically for laminar subcritical convection by Kelly & Pal (1978). Their linear analysis shows that the case with periodic temperature variation at flat walls is closely related to the problem with constant temperature but undulating surface. For small two-dimensional perturbations the heat-transfer rate increases with the square of the perturbation amplitude. These results were successfully used to test the present numerical integration scheme for laminar flows in Krettenauer & Schumann (1989*b*). Pal & Kelly (1979) also considered three-dimensional convection. They found that convection induced by two-dimensional thermal forcing becomes unstable with respect to three-dimensional disturbances, consisting of two sets of oblique rolls. Krettenauer & Schumann (1989*b*) found that such rolls also develop over wavy terrain.

Most previous LES studies considered flows over plane and homogeneous surfaces (Mason 1989; Moeng & Wyngaard 1989; Nieuwstadt 1990; Sykes & Henn 1989). The effects of inhomogeneous flat surfaces on the turbulent CBL have been investigated by Hadfield (1988), Schmidt (1988), Hechtel, Moeng & Stull (1990), and Graf & Schumann (1991) using LES. Hadfield (1988) observed a general increase of velocity

fluctuations due to an idealized two-dimensional surface heat-flux perturbation. Schmidt (1988) found a considerable increase of horizontal velocity fluctuations with increasing inhomogeneity but a small reduction in the vertical velocity component. Graf & Schumann (1991) supported this result from simulations in comparison with field observations including a weak mean wind. Hechtel *et al.* (1990) simulated an observed case of the CBL with weak mean wind including moisture effects and random surface properties; they found little influence of inhomogeneity on the turbulence statistics. Schädler (1990) found larger effects from variations in surface moisture at scales of the order 10 to 20 km using two-dimensional simulations. On the other hand, Garratt *et al.* (1990) found 'barely significant' changes in simulations of a sea breeze with random changes in surface temperature and surface roughness, when using a two-dimensional model with horizontal grid spacing of 7.5 km. Briggs (1988) reported on steady downdraughts of 0.4 times the convective velocity scale induced by inhomogeneities in urban areas within rural surroundings at horizontal scales of the order of 4 km. Recently, some results on LES of the CBL over a wavy surface were reported by Walko, Cotton & Pielke (1990).

From field observations of the structure of the atmospheric CBL, Kaimal *et al.* (1982) found that 'gently rolling terrain' does not seem to affect the turbulence spectra except for a 30% increase in the lengthscale of the spectrum of vertical velocity and a 60% reduction of the lengthscale of temperature. The terrain had an irregular shape with amplitude of about 50 m and horizontal scale of about 10 km while the boundary-layer depth was of order 1 km. Wilczak & Phillips (1986) found increased (by about 40%) vertical velocity variance over the same terrain, presumably because of shear induced by up-slope convection (J. Wilczak, personal communication 1991). Druilhet *et al.* (1983*b*) made measurements over both a homogeneous and a heterogeneous site with terrain elevations of 48 m standard deviation and a wavelength of about 2 km in CBLs with a depth between 540 and 1360 m. They found that dissipative and spectral lengthscales are shorter (about half) over complex domain while all other statistics show smaller differences. Jochum (1988) investigated the turbulent field in the CBL over hilly terrain with maximum height variation of 100 m at scales of about 10 km. She found small changes in vertical velocity variance and temperature fluxes at various scales and in the structure of updraughts in comparisons to previous results over flat terrain; the differences were largest in the lowest third of the CBL. Huynh, Coulman & Turner (1990) compared mean profiles of variances and fluxes of moisture, temperature and vertical velocity fluctuations in convectively mixed layers over homogeneous and over rugged terrain with amplitudes of order 100 m and wavelengths of order 1 km. They did not find any systematic differences in comparison to results obtained over homogeneous terrain. Hence, these experimental findings are approximately consistent, but the experimental studies did not explain why the effects of terrain appear to be small in most respects.

For the present study, we implement a subgrid-scale (SGS) model into the numerical scheme which uses terrain-following coordinates for accurate representation of the boundary conditions at the surface. The SGS model is similar to that used by Schmidt (1988), Schmidt & Schumann (1989), Ebert, Schumann & Stull (1989) and Schumann (1989). It is simplified in comparison to that used previously in that buoyancy enters the SGS model only through the transport equation of kinetic energy and not through a second-order closure for the SGS fluxes. This simplification was introduced because the previous scheme may violate realizability properties. Moreover, the anisotropy at SGS turned out to be small, at least above

the lowest grid layer and therefore it does not provide more accuracy (Schumann 1990, 1991) but requires more computational work. However, the model includes the buoyancy forcing in the budget of SGS kinetic energy, which is important and not included in the classical Smagorinsky model (see Nieuwstadt 1990). The method will be described in §2. For validation, the simulation results for a flat surface will be compared in §3.1 with the laboratory experiments of Adrian, Ferreira & Boberg (1986) in a water tank. The results for wavy surfaces will be described in the remainder of §3. Section 4 summarizes and discusses the results.

2. The simulation method

2.1. *Model equations*

As in Clark (1977), the equations of motion are formulated for the Cartesian velocity components $u_i = (u, v, w)$ as a function of curvilinear coordinates $\bar{x}^j = (\bar{x}, \bar{y}, \bar{z})$ which are related to the Cartesian coordinates $x_i = (x, y, z)$ according to the transformation $\bar{x} = x, \bar{y} = y, \bar{z} = \eta(x, y, z)$. Here,

$$\eta = H\frac{z-h}{H-h} \tag{1}$$

maps the domain above the wavy surface at height $h(x, y) = \delta \cos(2\pi x/\lambda)$ and below a plane top surface at $z = H$ onto a rectangular transformed domain. A plot of the transformed coordinates has been shown, for example, in Schumann & Volkert (1984) and Schumann *et al.* (1987). This non-orthogonal transformation is applicable for surface inclinations below about 45°. The code does contain more complex transformations to provide for variable resolution near the surface (Krettenauer 1991), but we do not use them because we found that this provides no advantages for convective cases (Sykes & Henn 1989; Nieuwstadt *et al.* 1991).

For an arbitrary scalar field ψ (including the individual Cartesian velocity components) the derivatives with respect to the Cartesian coordinates can be expressed as

$$\frac{\partial}{\partial x_i}\psi = \frac{\partial \bar{x}^r}{\partial x_i}\frac{\partial}{\partial \bar{x}^r}\psi \equiv G^{ri}\frac{\partial}{\partial \bar{x}^r}\psi. \tag{2}$$

Although we are not transforming vector or tensor quantities, we use the common tensor notation where upper indices correspond to contravariant coordinates. This simplifies comparisons with literature in which the tensor version is being used (Pielke 1984). The summation convention applies to repeated indices. The matrix G^{ij} of differential quotients was called a 'metric tensor' by Clark (1977) but this term has a different meaning in tensor calculus. For compactness, we avoid writing vertical and horizontal terms separately. Using the Jacobi determinant

$$V = (\det(G^{ij}))^{-1}, \tag{3}$$

allows derivatives to be transformed in a 'conservative form' (see e.g. Schumann & Volkert 1984) owing to the equality

$$V\frac{\partial}{\partial x_i}\psi = \frac{\partial}{\partial \bar{x}^r}(VG^{ri}\psi), \tag{4}$$

which holds for a restricted class of transformations, including the one considered in this paper (Krettenauer 1991).

With these definitions, the model equations are given by the continuity equation for constant density ρ,

$$\frac{\partial}{\partial \bar{x}^d}(\rho V G^{dq} u_q) = 0, \tag{5}$$

by the momentum balance in terms of the Cartesian velocity components u_i, pressure p, SGS momentum fluxes F_{ij}, volumetric expansion coefficient β, gravity g, and temperature T:

$$\frac{\partial}{\partial t}(\rho V u_i) + \frac{\partial}{\partial \bar{x}^d}(\rho V G^{dq} u_q u_i) = -\frac{\partial}{\partial \bar{x}^g}(V G^{gi} p) - \frac{\partial}{\partial \bar{x}^d}(G^{ds} V F_{is}) + \beta g \delta_{3i} T, \tag{6}$$

and by the heat balance in terms of temperature (for constant specific heat capacity)

$$\frac{\partial}{\partial t}(\rho V T) + \frac{\partial}{\partial \bar{x}^d}(\rho V G^{dq} u_q T) = -\frac{\partial}{\partial \bar{x}^d}(G^{dr} V Q_r), \tag{7}$$

where Q_i represents the SGS heat flux.

The diffusive fluxes of momentum are driven by the deformation of the velocity field

$$V D_{ij} = \frac{\partial}{\partial \bar{x}^r}(V G^{rj} u_i + V G^{ri} u_j). \tag{8}$$

For DNS, the diffusive fluxes are

$$V F_{ij} = -\rho \nu V D_{ij}, \tag{9}$$

$$V Q_i = -\rho \gamma \frac{\partial}{\partial \bar{x}^g}(V G^{gi} T). \tag{10}$$

For the LES we use

$$V F_{ij} = -\rho K_M V D_{ij} + \tfrac{2}{3}\delta_{ij} \rho V e, \tag{11}$$

$$V Q_i = -\rho K_H \frac{\partial}{\partial \bar{x}^g}(V G^{gi} T). \tag{12}$$

The turbulent diffusivities for momentum and heat are computed from

$$K_M = c_\nu e^{\frac{1}{2}} l, \quad K_H = c_\gamma e^{\frac{1}{2}} l, \tag{13}$$

with the mixing lengths related to the grid spacings $\Delta x, \Delta y, \Delta z$ in real space as appropriate for LES,

$$l = \min\{\tfrac{1}{3}(\Delta x + \Delta y + \Delta z);\ c_L(z-h)\}. \tag{14}$$

The second part becomes effective only in the lowest grid layer and accounts for the limitation of turbulent eddies by the lower surface at height $h(x, y)$. The diffusivities also depend on a characteristic velocity which we compute from the square root of the kinetic energy e of SGS turbulent motions. For this energy we solve the transport equation

$$\frac{\partial}{\partial t}(\rho V e) + \frac{\partial}{\partial \bar{x}^d}(\rho V G^{dq} u_q e) = -\tfrac{1}{2} F_{qr} V D_{qr} + \beta g (V Q_3) - \frac{\partial}{\partial \bar{x}^d}(G^{dr} V S_r) - c_{EM} \rho V \frac{e^{\frac{3}{2}}}{l}, \tag{15}$$

with diffusive fluxes

$$V S_i = -\rho \tfrac{5}{3} c_{3M} e^{\frac{1}{2}} l \frac{\partial}{\partial \bar{x}^g}(V G^{gi} e). \tag{16}$$

The model contains various coefficients for which we use the values found to be appropriate by Schmidt (1988),

$$c_{3M} = 0.2, \quad c_{EM} = 0.845, \quad c_\nu = 0.057, \quad c_\gamma = 0.136, \quad c_L = 1. \tag{17}$$

The coefficients c_ν and c_γ are slightly smaller than those derived and used by Schmidt & Schumann (1989) and Schumann (1990). Our experience with variations in the coefficients (Schmidt & Schumann 1989), tests with various SGS models (Schumann 1991) and comparisons between LES results from different numerical methods and different SGS models (Nieuwstadt *et al.* 1991) show that even a doubling of important SGS coefficients changes the flow statistics only little.

2.2. *Discretization*

The differential equations are approximated by finite differences. In space we use an equidistant staggered grid which allows for a compact representation of the continuity equation, at least for Cartesian coordinates. The momentum equation is integrated using the Adams–Bashforth scheme in time and second-order finite differences in space. This scheme conserves momentum and, to a high degree, kinetic energy. The transport equations for temperature and SGS kinetic energy are integrated using the second-order upwind scheme proposed by Smolarkiewicz (1984) which guarantees positivity and exhibits only weak numerical diffusion. The pressure is computed implicitly such that the continuity equation is satisfied after each time step.

Some details are reported below. Here, Δt denotes the time-step increment. Superscripts (n) identify the time-step number. Intermediate results between the time steps are denoted by a tilde. Finite differences in space are denoted by δ_r; e.g. $\partial(\ldots)/\partial \bar{x}^r \approx \delta_r\{\ldots\}$.

The temperature at the time level $t^{(n+1)}$ is computed explicitly,

$$\rho V T^{(n+1)} = \rho V T^{(n)} - \Delta t \delta_d \{\rho V G^{dq} (u_q T)^{(n)} + G^{dr} V Q_r^{(n)}\}. \tag{18}$$

Here, the advective fluxes with the transport velocity $\rho V G^{dq} u_q$ are computed according to the Smolarkiewicz scheme. The same scheme is used to compute the advective parts of the SGS-energy transport,

$$\rho V \tilde{e} = \rho V e^{(n)} - \Delta t \delta_d \{\rho V G^{dq} u_q e^{(n)} + G^{dr} V S_r^{(n)}\}. \tag{19}$$

To this intermediate result we add the energy production rate by shear and buoyancy

$$\rho V e^{(n+1)} = K_E \rho V \tilde{e} - \Delta t (\tfrac{1}{2} F_{rs} V D_{rs}^{(n)} - \beta g V Q_3^{(n)}) \tag{20}$$

and account for the action of dissipation by the damping factor,

$$K_E = \left(1 + \tfrac{1}{2} c_{EM} \frac{(e^{\frac{1}{2}})^{(n)}}{l} \Delta t\right)^{-2}. \tag{21}$$

This factor describes the exact solution in a purely dissipating situation and avoids negative energy results in regions with strong dissipation.

With respect to velocity, we first compute accelerations

$$(b_i)^{(n)} = \delta_d \{\rho V G^{dq} (u_q u_i)^{(n)} + G^{ds} V F_{is}^{(n)}\}, \tag{22}$$

which give an intermediate velocity according to the Adams–Bashforth scheme

$$\rho V \tilde{u}_i = \rho V u_i^{(n)} - \Delta t (\gamma_0 (b_i)^{(n)} - \gamma_1 (b_i)^{(n-1)} + \delta_g \{V G^{gi} (p)^{(n)}\} - \beta g \delta_{3i} (T)^{(n+1)}), \tag{23}$$

with $\gamma_0 = \frac{3}{2}$, $\gamma_1 = \frac{1}{2}$. Note that the buoyancy term is calculated from the most recent temperature result; this is necessary for numerical stability when temperature is computed from an Euler-type time-integration scheme like that of Smolarkiewicz (1984). In order to obtain the final velocity field, $\tilde{u}_i$ has still to be corrected by means of the gradient of the pressure change Δp,

$$\rho V u_i^{(n+1)} = \rho V \tilde{u}_i - \Delta t \, \delta_g \{ V G^{gi} (\Delta p) \}, \tag{24}$$

such that it satisfies the continuity equation. The new pressure result is

$$p^{(n+1)} = p^{(n)} + \Delta p. \tag{25}$$

The pressure change Δp is the solution of the linear system of equations corresponding to a discretized elliptic partial differential equation

$$\frac{1}{\Delta t} \delta_d \{ \rho V G^{dq} \tilde{u}_q \} = \delta_d \{ G^{dq} \delta_g \{ V G^{gq} (\Delta p) \} \}, \tag{26}$$

or the equivalent operator equation

$$q = \mathrm{L}\{\Delta p\}, \tag{27}$$

in which q enters as a function of the divergence of the intermediate field and L denotes the Laplace operator in the transformed coordinates.

As in Schumann & Volkert (1984), the elliptic equations are solved iteratively,

$$\mathrm{M}\{\Delta p^{\nu+1} - \Delta p^{\nu}\} = q - \mathrm{L}\{\Delta p^{\nu}\}, \quad \Delta p^{\nu=1} = 0, \tag{28}$$

for $\nu = 1, \ldots, 5$. Here M is an operator which is obtained from L if the surface height $h(x, y)$ is replaced by its horizontal mean value. M can be inverted by means of fast direct solvers (Schumann & Sweet 1988). Five iterations are sufficient to reduce the divergence to order 10^{-5} of w_*/H, which is defined below.

2.3. *Boundary conditions*

At the lateral boundaries, cyclic boundary conditions are used. At the bottom surface, we implement boundary conditions which approximate the no-slip condition with zero tangential velocity and prescribed heat flux. The method prescribes constant heat flux per horizontal unit area. This should approximate a sun in the zenith with uniform heating over a horizontal area. No specific temperature boundary conditions are needed for given heat fluxes. In the DNS, the no-slip condition is implemented by second-order finite differences. In the LES, the Monin–Oboukhov relationships are used for that purpose as described in Schmidt & Schumann (1989). The pressure boundary condition at the surface is obtained from (24) such that the normal velocity

$$G^{3q} \rho V u_q^{(n+1)} = 0 \tag{29}$$

remains zero at the surface. In Cartesian coordinates this implies a Neumann boundary condition for the pressure at the surface. In curvilinear coordinates, the numerical discretization causes a coupling between the pressure values at neighbouring surface grid points so that a linear system has to be solved (Clark 1977; Schumann & Volkert 1984); for details see Krettenauer (1991). At the rigid top surface the vertical momentum and heat fluxes are set to zero.

It should be noted that laminar convection over flat surfaces with these boundary conditions starts at a critical Rayleigh number with circulations at infinite horizontal wavelengths (Fiedler 1989; Krettenauer 1991). However, as shown by Fiedler (1989),

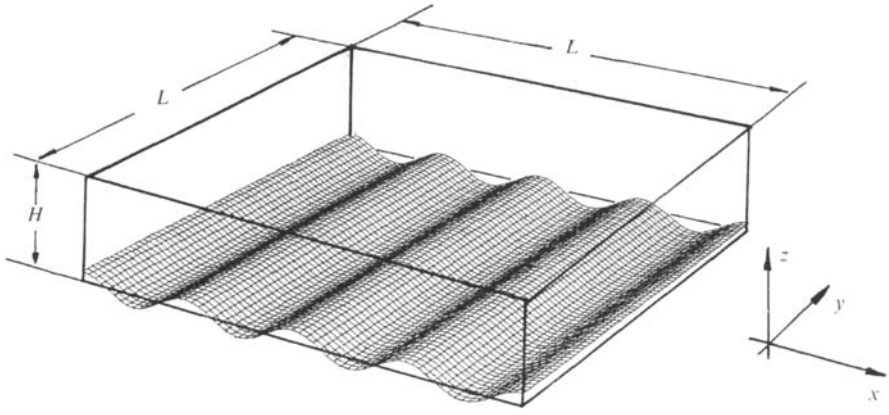

FIGURE 1. Perspective sketch of the computational domain in three dimensions showing the sinusoidal surface wave in the x-direction; the surface height is constant in the y-direction. In the example, the wavelength is $\lambda = H$, the wave amplitude is $\delta = 0.1H$, and the lateral domain size is $L = 4H$.

	Case	L/H	λ/H	δ/H	Grid cells	t_{max}	N	CPU s
Set D:	D1014	4	1	0.1	$64\times64\times16$	35	3500	3100
DNS	D1024	4	2	0.1	$64\times64\times16$	35	3500	3100
	D1044	4	4	0.1	$64\times64\times16$	35	3500	3100
	D00U4	4	∞	0.0	$64\times64\times16$	35	3500	3100
	D1514	4	1	0.15	$64\times64\times16$	35	3500	3100
	D1018	8	1	0.1	$128\times128\times16$	35	3500	10700
	D1088	8	8	0.1	$128\times128\times16$	35	3500	10700
Set L:	L1014	4	1	0.1	$64\times64\times16$	35	3500	4400
LES	L1024	4	2	0.1	$64\times64\times16$	35	3500	4400
	L1044	4	4	0.1	$64\times64\times16$	35	3500	4400
	L00U4	4	∞	0.0	$64\times64\times16$	35	3500	3400
	L1514	4	1	0.15	$64\times64\times16$	35	3500	4400
	L1018	8	1	0.1	$128\times128\times16$	35	3500	14700
	L1088	8	8	0.1	$128\times128\times16$	35	3500	14700

TABLE 1. Model parameters for the various cases: t_{max} represents the final integration time in units of t_*; N denotes the number of integration steps; the computer time refers to runs on a CRAY-YMP. The 'string' that denotes each case is defined in the text

shorter wavelengths develop more quickly at supercritical Rayleigh numbers. By means of LES of the CBL over flat terrain, Krettenauer & Schumann (1989*a*) found that fully turbulent convection results in practically the same horizontal scales regardless of prescribing the heat flux or the temperature at the surface.

2.4. *Initialization and parameters*

We report below results obtained from a set D of direct simulations and a set L of large-eddy simulations, see table 1. The cases are denoted by a string 'mddlL', where m ∈ D, L, identifies the method, dd ∈ 00, 10, 15, the wave-amplitude in percent, l ∈ U, 1, 2, 4, 8, the wavelength (U for undefined), and L ∈ 4, 8 denotes the domain size in units of H. Figure 1 depicts the computational domain and the grid on the wavy surface for case L1014. In order to point out that the undulation is strong, we

note that the maximum slope $2\pi\delta/\lambda$ reaches 0.942 with an inclination of 43° for $\delta/H = 0.15$. For set L, we specify the surface roughness height (which enters the Monin–Oboukhov relationships for momentum and heat transfer) as $z_0 = 10^{-4}H$.

The results are normalized by the characteristic velocity, height, temperature and time scales,

$$w_* = (\beta g Q_S H)^{\frac{1}{3}}, \quad H, \quad T_* = Q_S/w_*, \quad t_* = H/w_*, \tag{30}$$

respectively, which are the 'convective' scales as proposed by Deardorff (1970). Here, β is the volumetric expansion coefficient, g is the acceleration due to gravity, Q_S is the prescribed vertical temperature flux at the surface, and H is the mean height of the flow domain. In the atmosphere, typical values are of the order $w_* = 1.3$ m s^{-1}, $H = 1000$ m, $T_* = 0.05$ K, $t_* = 13$ min.

The set D is run for a Reynolds number Re and Prandtl number Pr,

$$Re = w_* H/\nu = 100, \quad Pr = \nu/\gamma = 0.7. \tag{31}$$

The Reynolds number is related to a Rayleigh number $Ra = \beta g Q_S H^4/(\nu\gamma^2)$ by $Ra = Re^3 Pr^2$, which equals 490000 in the present case. Laminar convection sets in when this Rayleigh number exceeds the critical value 720 (Krettenauer 1991). The corresponding critical Reynolds number for $Pr = 0.7$ is 11.4. The Reynolds number value is selected based on the experience of Krettenauer & Schumann (1989*b*) who performed direct simulations for Reynolds numbers of 100, 150, and 250. The value $Re = 100$ is large enough to produce turbulent solutions but small enough to have all scales resolved with the selected discretization. The horizontal and vertical resolution are both finer than the requirements $4.758 Pr^{\frac{1}{2}} Ra_{\Delta T}^{-0.3205}$ and $1/(2Nu)$, respectively (Grötzbach 1983), where $Ra_{\Delta T} = g\beta\Delta T H^3/(\nu\gamma) = Re^2 Pr \Delta T/T_*$ is the more common Rayleigh number based on the temperature difference between the surface and the bulk of the fluid layer, and Nu is the related Nusselt number. From the results of the present simulations we obtain $Ra_{\Delta T} \approx 55000$, and $Nu \approx 5$.

From the final LES results we estimate that the average SGS kinetic energy is about $0.1 w_*^2$. The local SGS diffusivity is certainly variable but the average turbulent diffusivity for momentum can be computed from (13), and this value can be used to quantify an equivalent Reynolds number which measures the importance of such diffusivity. Its value is 888. It is large enough that fully turbulent solutions can be expected, but finite. In this sense one may question whether the LES truly represents the infinite-Reynolds-number solutions at large scales. However, LES at least widens the range of scales submitted to significant excitation. Moreover, all the insight we have obtained so far from comparing LES results with measurements at very high Reynolds numbers, e.g. in the atmosphere (Schmidt & Schumann 1989), indicates that the LES at least provides a good approximation for this limit.

In the laboratory experiment of Adrian *et al.* (1986) the scale values for the case with largest heat flux $Q_S = 0.450$ K mm/s are $Re = 1736$, $w_* = 6.96$ mm s^{-1}, $H = 200$ mm, $T_* = 0.082$ K, $t_* = 29$ s.

The initial conditions prescribe zero mean velocities, constant mean temperature and constant SGS kinetic energy. Random perturbations are added to the temperature and velocity field to initiate three-dimensional motions which eventually become turbulent. The details of these disturbances are unimportant for the final statistics but the actual values are

$$T/T_* = 10 + 0.1(1 - z/H)\ \text{ranf}(), \quad w/w_* = (1 - z/H)\ \text{ranf}(). \tag{32}$$

Here, ranf ( ) is a random number generator with equal distribution between -0.5 and 0.5. The mean value 10 of the initial temperature, which is large in comparison

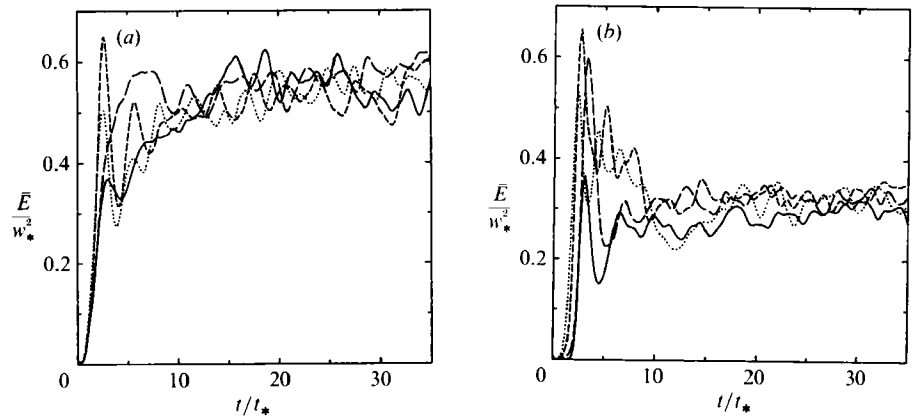

FIGURE 2. Spatially averaged kinetic energy (normalized by w_*^2) versus time t/t_* for (*a*) LES cases and (*b*) DNS cases: ——, L00U4/D00U4; ....., L1014/D1014; ----, L1024/D1024; –-, L1044/D1044.

to the fluctuations, has been selected because the (small) numerical diffusion in the (nonlinear) Smolarkiewicz scheme gets even smaller for scalar fields with larger mean values (Smolarkiewicz 1984; Schumann *et al.* 1987; Ebert *et al.* 1989).

Ideally, the computations should run until steady-state statistics are obtained. In the present computations, the larger the wavelength λ, the longer will be the time required to reach that state, because the time required to mix out horizontal variations increases with λ. For that reason we checked some statistics and ran the computations until the rather large final time of $35t_*$. For an atmosphere of 1000 m thickness and a temperature flux $Q_S = 0.1$ K m s^{-1} (heat flux of about 100 W m^{-2}) this corresponds to about 6 h. Schmidt & Schumann (1989) ended their simulations of the atmospheric CBL at $t = 7t_*$. Hence we can expect that our final results are close to steady state.

Figure 2 shows the temporal development of the kinetic energy averaged over the total computational domain for four cases of the LES and the DNS. We see that the initial energy provided by the random perturbations is small. The energy increases at about the same rate in the cases with and without a wavy surface. This suggests that the longer circulations cells over longer surface waves, which have larger inertia, experience a correspondingly stronger forcing from buoyancy, so that their timescale is about the same. In the initial period the energy reaches rather large values according to dominant roll circulations driven by the wavy surface. Later, however, the flow structure becomes more random with increased dissipation and the energy tends to an asymptotic level at times before $t \leqslant 15t_*$ for all cases (including those with $\lambda = 8H$, which are not included in the plots). The final energy level is larger in the LES cases than in the DNS cases because of stronger dissipation at lower Reynolds numbers. We observe that even this integral quantity does not reach a strictly steady state. Instead we observe fluctuations at timescales of the order of a few convective time units around an apparently existing asymptotic value. These fluctuations are explained by the finite domain size. In the simulations kinetic energy is exchanged forth and back between small and large scales. Since the domain contains only a finite number of large scales, the volume average differs from a true ensemble mean value. Strict steady state can be achieved in such simulations only if the domain size is many orders of magnitude wider than the largest important scales of motion. For the same reasons, very large averaging times or distances are also required in

experiments (Lenschow & Stankov 1986). In fact, the requirements are more stringent in one-dimensional averages than in two or three dimensions because the latter cover more independent events at large scales. Ensemble mean values with smaller statistical errors could be obtained by averaging over the results from several simulations which are obtained for different sets of random perturbations in the initial conditions (Hadfield 1988). However, this is computationally an expensive approach. Therefore, we proceed pragmatically and present results which are averages over the last five time units of the simulations. A further check of steady state will be obtained by inspection of the profile of vertical heat flux which should be a linear function of height in steady state (see below).

3. Results

3.1. *LES of the flat case; comparison with measurements*

The present method has been validated by comparison to atmospheric and laboratory measurements for a CBL which is topped by a stable fluid layer (Schmidt & Schumann 1989). These comparison have shown that the results, for high grid resolution ($160 \times 160 \times 48$), are at least as accurate as available measurements. Graf & Schumann (1991) have compared LES results with recent field observations for a CBL with non-zero mean wind; they found good comparisons for much coarser grids. Further parameter studies (Schumann 1991) and comparisons of the LES results from four different methods (Nieuwstadt *et al.* 1991) have shown that mean profiles of first-, second- and third-order moments of turbulence quantities in the mixed layer of the CBL can be accurately represented even when using only $40 \times 40 \times 15$ grid cells in the CBL covering a domain of $4 \times 4 \times 1.5$ boundary-layer depths. It still remains to validate the present code, because it contains many coding changes in order to treat curvilinear coordinates, contains a simplified SGS-model in comparison to that of Schmidt & Schumann (1989), and is applied with a lid at the top of the mixed layer instead of a stable fluid layer.

For this purpose, the LES results will be compared to the laboratory results obtained by Adrian *et al.* (1986) for non-penetrative convection between a heated lower and an adiabatic rigid upper surface, which is the same as we consider in this study except that we use a free-slip top surface. Also, Sykes & Henn (1989) compared their LES results with some of the measurements. Sorbjan (1990) applied the same data to calibrate similarity laws which approximate atmospheric cases. The experimental data are obtained for Re between 552 and 1736. The experimental results, scaled by the convective scales, are virtually independent of Re and therefore assumed to be representative of a case with very large Reynolds number. Hence, we compare these results to our LES, case L00U4. Subsequently we compare mean profiles which are obtained by averaging over horizontal surfaces and over the time period $t/t_* = 30$ to 35, as a function of the vertical coordinate z, with the experimental data.

Figure 3 shows the vertical profile of mean kinetic energy. The SGS part amounts to less than 20% of the total energy and, hence, the results can be classified as LES in spite of the still rather coarse grid resolution. The energy is large near the upper surface because of the free-slip condition; it is also large near the lower surface because there the buoyancy forcing takes its maximum value and the surface friction is small in comparison to internal turbulent mixing.

The mean temperature has increased from its initial value of 10 (in units of T_*) to 42.5 because of constant heating in the integration period, as required for heat

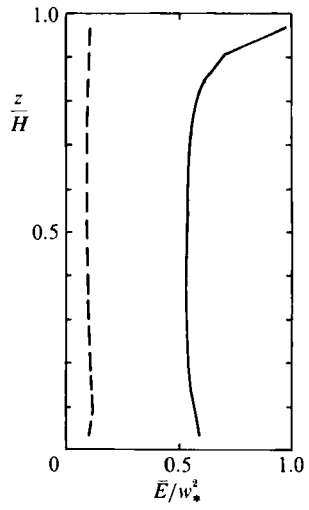

FIGURE 3. Normalized mean kinetic energy $\bar{E} = \frac{1}{2}\overline{u_i'^2}$ of turbulent motions versus normalized height z/H, for the LES case with a flat surface: ---, SGS-contribution; ——, total (SGS plus resolved) energy. The results are normalized with the convective velocity w_* and the height H of the fluid layer. The mean values represent averages over horizontal planes and over the time period from $30t_*$ to $35t_*$.

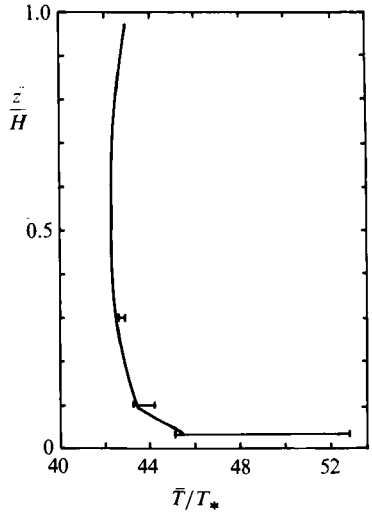

FIGURE 4. Mean temperature profile versus height z/H, for the LES case with a flat surface: ——, LES-result; 'error' bars enclose the experimental data for three heights from Adrian *et al.* (1986). The results are normalized with the convective temperature T_* and the height H of the fluid layer.

conservation. The temperature profile is shown in figure 4. In this figure, the bars denote the range of experimental results. We find satisfactory agreement. The measured temperature at $z/H = 0.03$ exhibits large scatter but is larger because of the finite Reynolds number and the rather large Prandtl of water (about 5), in which the data were taken. The temperature increases in the upper part of the layer with increasing height. This counter-gradient heat transport is caused by narrow and fast rising thermals which transport heat from the lower surface directly up to the upper part of the fluid layer from where the remainder of the fluid within the mixed layer is heated by turbulent diffusion and sinking warm fluid from above.

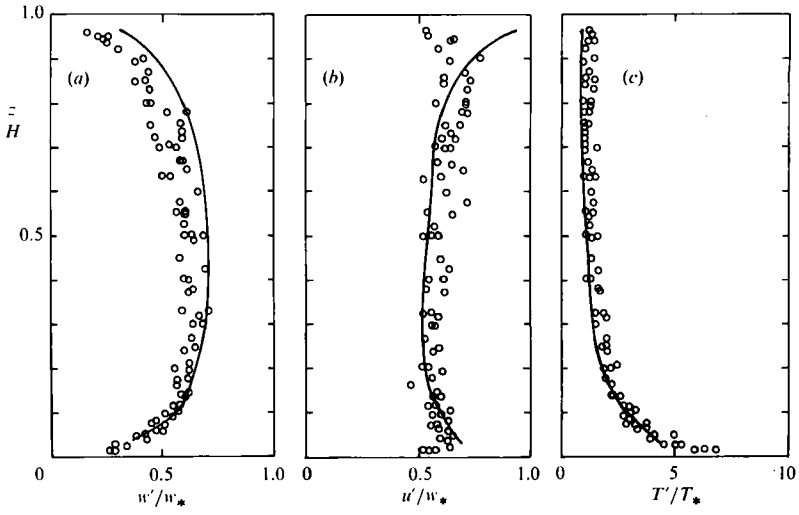

FIGURE 5. Root-mean-square fluctuations of (*a*) vertical velocity w', (*b*) horizontal velocity u', and (*c*) temperature T', versus height for the LES case with a flat surface: ——, LES results (including SGS contributions); ○, the experimental results of Adrian *et al.* (1986).

In figure 5 we compare root-mean-square (r.m.s.) values of vertical and horizontal velocity fluctuations and of temperature fluctuations as computed from the LES with the measured results. The scatter of the experimental data characterizes approximately the standard deviation of these measurements. The vertical velocity fluctuations are largest in the mid-channel, as expected, and only a little larger in magnitude than the values observed in the CBL. Schmidt & Schumann (1989) pointed out that w' increases slightly with increasing stability; in this sense, the rigid top wall represents the infinite-stability case. The measurements are close to the computed results. The systematic deviation to lower measured values in the upper part is caused by friction at the top surface. Similar comments apply to the horizontal velocity fluctuations. The temperature fluctuations are largest near the heated wall. A lower limit is easily obtained assuming complete correlation with vertical velocity fluctuations, $T' > \overline{w'T'}/w'$. Hence, T' is large in particular near the lower surface where small w' fluctuations are related to a large heat flux. Most of these fluctuations originate from very small-scale turbulent eddies, as is known for atmospheric boundary layers (Schmidt & Schumann 1989). Nevertheless, the LES captures this effect quite well. Overall, figure 5 shows excellent agreement between LES and experiment. Sykes & Henn (1989) used the same data as shown in figure 5 to test their LES for various grid discretizations including variable grid spacing in the vertical direction. They found similar agreement with the data as we obtain for constant vertical grid spacing.

The vertical temperature flux and the correlation coefficient of vertical velocity and temperature fluctuations are shown in figure 6. The measured data underestimate the flux. This is most obvious near the lower surface because there the normalized flux is unity by definition. This fact suggests that the LES gives higher accuracy than the measurements. The flux profile decreases linearly with height, as required for a steady state with constant heating rate according to the vertical divergence of the flux. The entrainment flux, which usually acts in atmospheric cases, is absent for the present case because of the rigid lid. The correlation coefficient is quite high. Druilhet

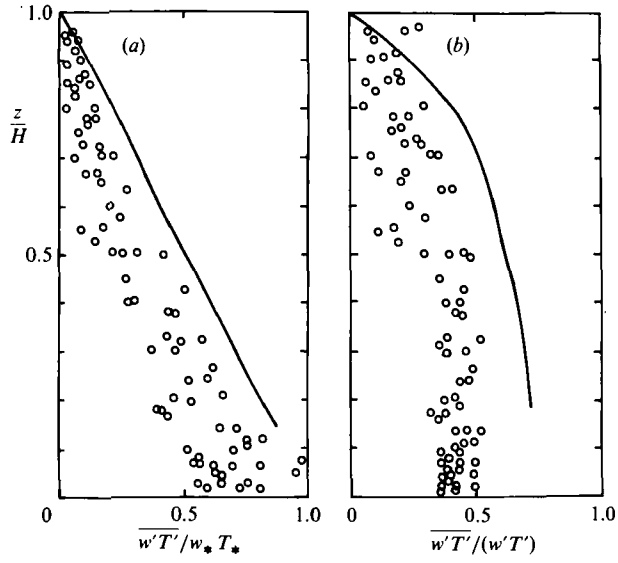

FIGURE 6. Turbulent temperature flux and correlation coefficient versus height for the LES case with a flat surface. (*a*) Flux normalized by surface temperature flux, (*b*) flux normalized by the r.m.s.-fluctuations of vertical velocity and temperature. ——, The sum of resolved and SGS contributions; ○, the experimental results of Adrian *et al.* (1986).

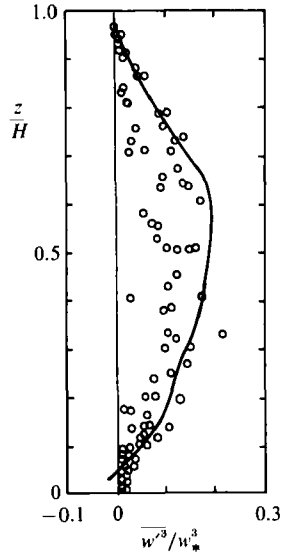

FIGURE 7. Vertical velocity cubed versus height for the LES case with a flat surface: ——, resolved contributions; ○, the experimental results of Adrian *et al.* (1986).

et al. (1983*a*) find a correlation coefficient of 0.5 in the lower 30% of an atmospheric CBL and smaller values above that height. The large correlation coefficient reveals that most of the motions are effective in transporting heat.

The third-order moment of the vertical velocity, shown in figure 7, is of importance with respect to vertical transport of kinetic energy (in the vertical velocity component). Its value is positive throughout the mixed layer and this indicates that the flow structure is composed of narrow updraughts with large upward velocity

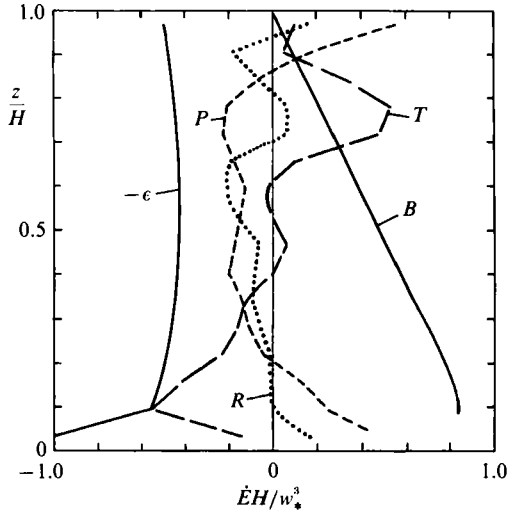

FIGURE 8. Contributions to the budget of kinetic energy versus height for the LES case with a flat surface: $B = \beta g\overline{w'T'}$, buoyancy flux; $T = -\partial\frac{1}{2}\overline{w'u'^2}/\partial z$, divergence of turbulent energy transport; $P = -\partial\overline{w'p'}/\partial z$, divergence of pressure energy transport; $\epsilon = c_{\epsilon M}\overline{e}^{\frac{3}{2}}/l$, modelled dissipation rate; and $R = \partial E/\partial t = B + P + T - \epsilon$, residuum. The results are obtained for $t = 30t_*$, and plotted in the normalized form.

surrounded by wide and slow downdraughts. The magnitude of this quantity is only a few percent smaller than that found for the CBL. In the CBL, we expect a larger energy transport in order to balance the increased energy sink from entrainment at the inversion. The LES shows a small but negative value in the lowest grid cell. This result should not be considered as realistic and is probably an effect of too large a dissipation rate near the surface, as discussed by Schmidt & Schumann (1989) (see also Nieuwstadt *et al.* 1991). Above the surface layer, the experiment seems to underestimate the energy flux. Our LES results are also very close to the DNS results reported by Moeng & Rotunno (1990) for the same boundary conditions. For a Reynolds number $Re = 139$, they find about the same profiles of variances and cubed values of vertical velocity as we showed in figures 6 and 7. This confirms again the independence of these statistics of the Reynolds number within the fully turbulent regime.

These results enter the energy budget. Figure 8 shows the complete budget of kinetic energy as computed from the LES. It shows, as expected, energy production by buoyancy which decreases linearly with height. On average, the production rate equals the dissipation rate ϵ, but the dissipation rate is smaller than the production rate in the lower half of the layer. Consequently, there is upward energy transport by vertical motions (T) whereas the pressure acts counter this transport. The residuum characterizes the accuracy of these budget results. (As an exception, for technical reasons, the results in figures 8 and 9 are obtained from the LES-results at $t = 30t_*$ without time averaging.) For steady state, the mean value of the dissipation should be exactly equal to the mean buoyancy forcing, i.e. equal to $0.5w_*^3/H$. For this particular time, the dissipation is little larger, and figure 2 shows, in fact, decreasing energy at $t = 30t_*$. In passing, we note that the domain averages $\epsilon \approx 0.5w_*^3/H$, and $E \approx 0.6w_*^2$ imply, for $z > 0.1H$, a dissipation scale $L_\epsilon = E^{\frac{3}{2}}/\epsilon \approx 0.93H$, and this value is only little larger than the results obtained for the CBL (Schumann 1991).

In figure 9, we compare some components of the energy budget with measured

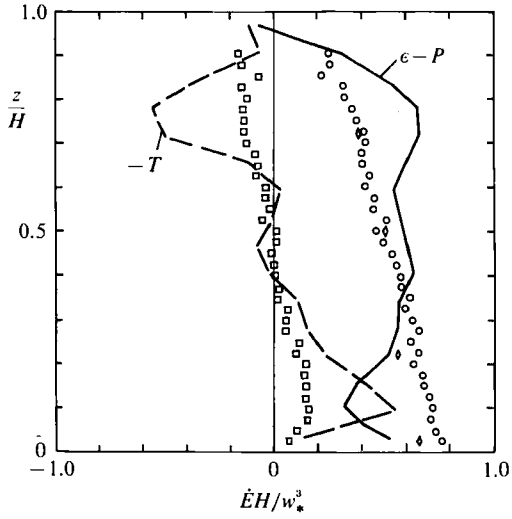

FIGURE 9. Comparison of parts of the budget of kinetic energy as computed by the LES for a flat surface (curves) with experimental data (symbols) by Adrian *et al.* (1986) versus height, T, P and ϵ are defined in the caption to figure 8. The results are obtained for $t = 30t_*$, and plotted in the normalized form. In the experiment, $\epsilon - P$ is determined as the residuum from the measured parts of the energy budget.

results. With respect to buoyancy forcing we refer to figure 6(*a*), where we have already noted that the measurements underestimate the forcing considerably (by about 30%). Also the flux $\overline{w'^3}$ appears to be underestimated by the measurements, see figure 7. Therefore, it is not surprising to find considerable differences between measured and computed divergences of vertical turbulent fluxes, $-T$ in figure 9. The figure shows also $\epsilon - P$. The symbols represent the residuum from the other measured results, assuming steady state. In view of these difficulties in the experiment, we cannot expect better agreement.

In conclusion, the comparison between the LES results for the plane surface with the experimental results from Adrian *et al.* (1986) shows that the LES results can be taken to be as reliable as such measurements.

3.2. *Mean profiles and phase averages over wavy terrain*

In this section we investigate the influence of the surface undulation on the turbulent convection in terms of mean profiles which are averages at constant transformed coordinates $\eta = \text{const}$, see (1), and averaged in addition over the last five time units. Figure 10 shows results from the DNS and figure 11 corresponding results from the LES. Both sets of curves are similar in many respects. The main difference is the reduced horizontal velocity variance and kinetic energy near the lower surface in the DNS because of increased viscous friction. The same reason explains why the profiles of horizontal variances look asymmetric in the DNS results but more symmetric in the LES. In the DNS the surface undulation causes largest changes in the vertical velocity variance, see figure 10(*c*), whereas in the LES the undulation effect is largest in the x-component of the velocity variance, see figure 11(*a*). In both simulations, the horizontal variances increase with wavelength in the x-direction while that in the y-direction is reduced. This is consistent with an increased excitation of rolls with axes parallel to the surface crests. However, the reduction in v is less systematic than the increase in u-variance. For short surface waves, the variance $\overline{v'^2}$ is larger than $\overline{u'^2}$, in

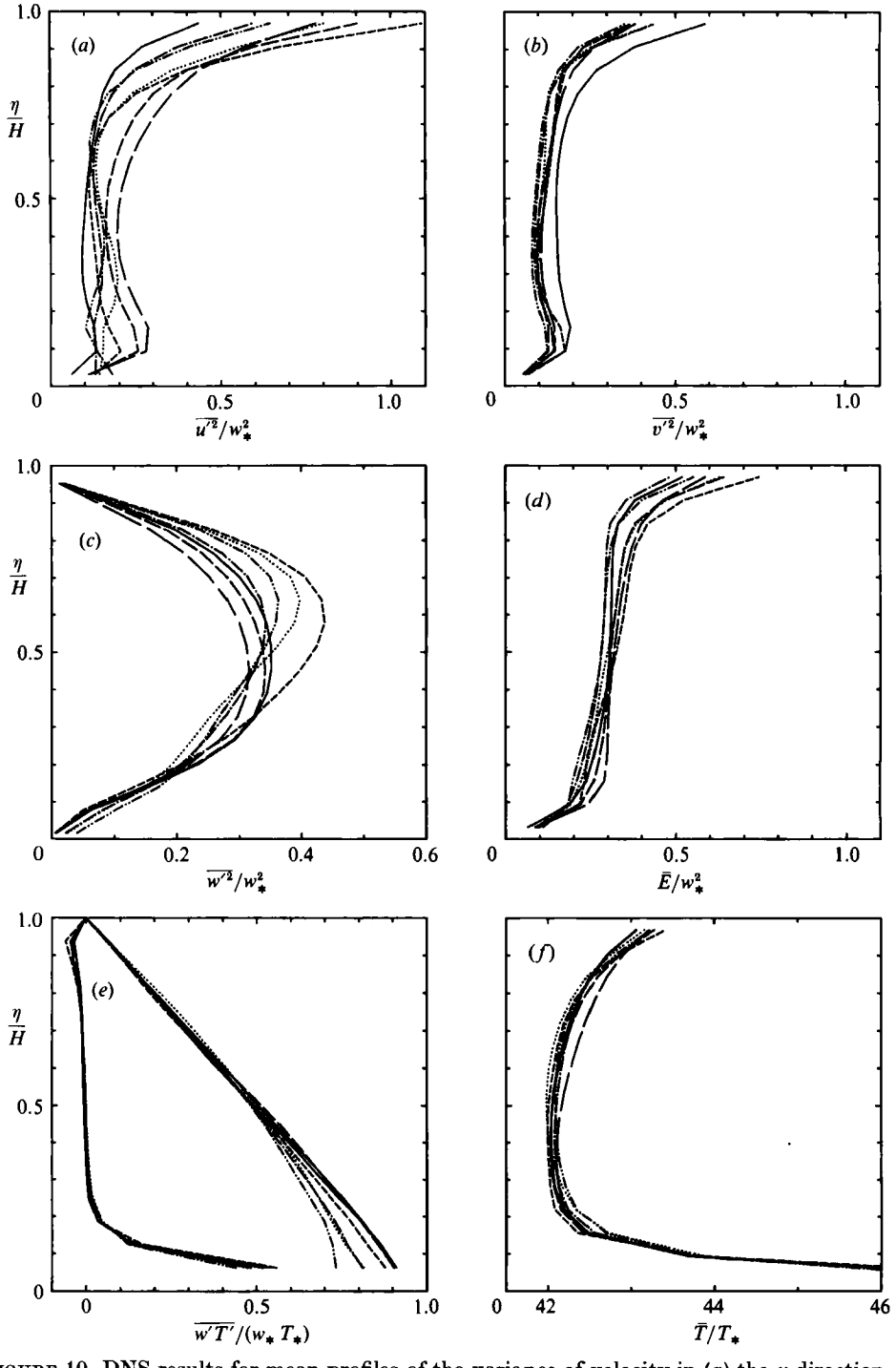

FIGURE 10. DNS results for mean profiles of the variance of velocity in (*a*) the *x*-direction, (*b*) the *y*-direction, (*c*) the *z*-direction; (*d*) kinetic energy of turbulent motions; (*e*) vertical heat flux (diffusive and total contributions); (*f*) mean temperature. ·····, D1014; - - - - - -, D1024; ——, D1044; ——, D00U4; –·–·–·, D1514; – – – –, D1018; ————, D1088.

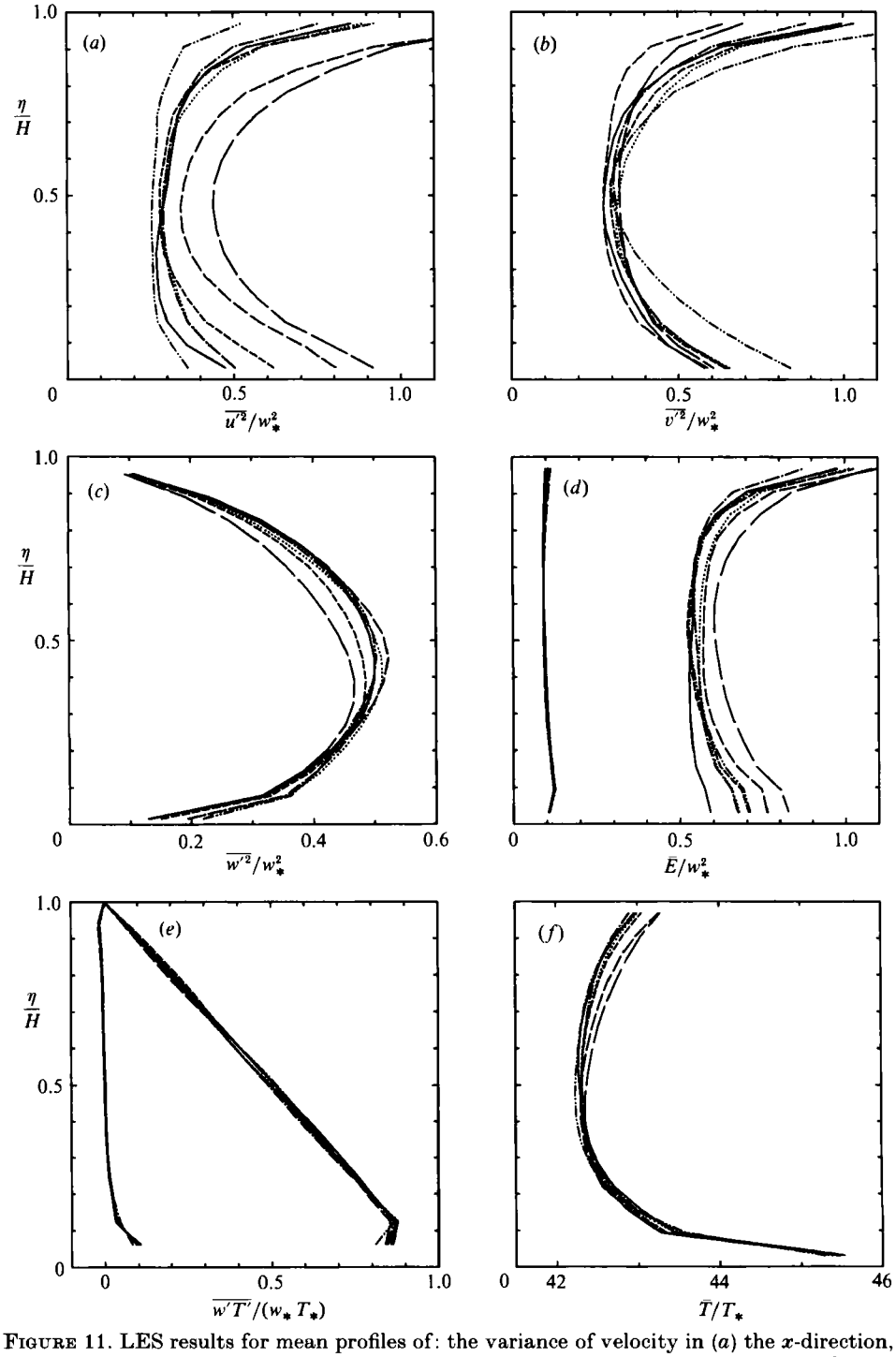

FIGURE 11. LES results for mean profiles of: the variance of velocity in (*a*) the *x*-direction, (*b*) the *y*-direction, (*c*) the *z*-direction; (*d*) kinetic energy of turbulent motions; (*e*) vertical heat flux; (*f*) mean temperature. In (*d*) and (*e*) the SGS parts are shown beside the total results. · · · · ·, L1014; - - - - - -, L1024; ——, L1044; ———, L00U4; —·—·—, L1514; — — —, L1018; ————, L1088.

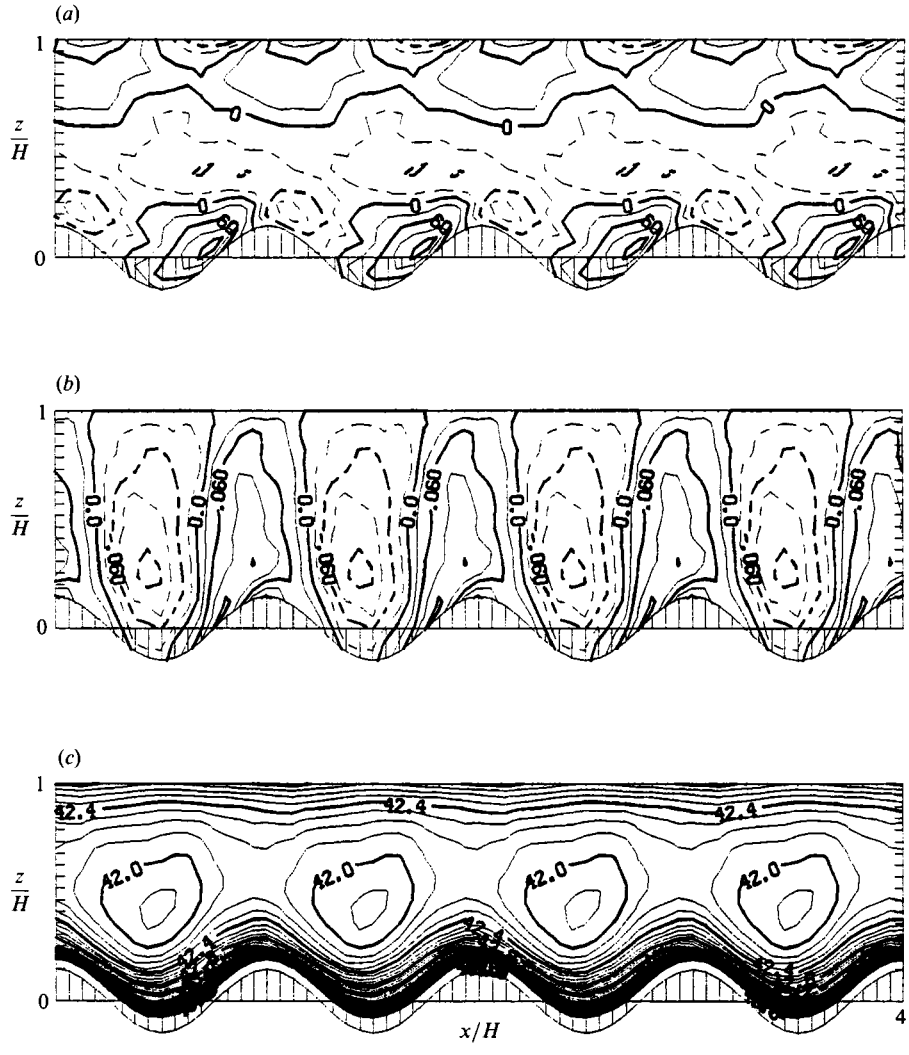

FIGURE 12. Contour plots of phase- and time-averaged mean fields for case L1514 ($\delta/H = 0.15$, $\lambda/H = 1$, $L/H = 4$). (*a*) Horizontal velocity u, increment $0.03w_*$; (*b*) vertical velocity w, increment $0.03w_*$, (*c*) temperature T, increment $0.06T_*$.

particular near the bottom and top boundaries, which indicates that there are strong rolls with axes in the x-direction. This is the first indication of 'secondary rolls', which will be discussed below. The kinetic energy profiles change rather little. This is to be expected because the profile of the mean buoyant forcing is roughly the same in all cases and also the dissipation will be little affected by changes at large scales. An increase of energy in the large scales implies, therefore, a decrease of the parts with turbulent motion. This explains the decrease of v' and also of w' variance with increasing wavelength of the surface wave. For short wavelengths, $\overline{w'^2}$ might become larger than over flat terrain, in particular for the low-Reynolds-number case, see figure 10(*c*). The results for steep but short surface waves (D1514 and L1514) are generally very close to those for a flat surface (full curves). The total heat flux (resolved plus SGS part or conductive part) is affected very little by orography because of prescribed heat flux at the surface and constant mean divergence in

Case	L1014	L1024	L1044	L00U4	L1514	L1018	L1088
u_{max}/w_*	0.0856	0.213	1.308	0	0.129	0.084	1.151
w_{max}/w_*	0.062	0.170	0.832	0	0.127	0.055	0.394
$-w_{min}/w_*$	0.074	0.136	0.464	0	0.132	0.045	0.250
$\tilde{u}_*/w_*$	0.119	0.121	0.125	0.113	0.120	0.118	0.127
$\Delta T/T_*$	50.0	49.4	49.0	49.1	51.0	50.1	48.8
Case	D1014	D1024	D1044	D00U4	D1514	D1018	D1088
u_{max}/w_*	0.316	1.114	1.101	0	0.398	0.320	0.602
w_{max}/w_*	0.207	0.936	0.658	0	0.379	0.240	0.174
$-w_{min}/w_*$	0.273	0.557	0.357	0	0.339	0.259	0.321
$\Delta T/T_*$	7.5	8.2	7.9	7.8	7.1	7.4	7.9

TABLE 2. Mean circulation and heat transfer results: u_{max}, w_{max}, w_{min} are the extreme values of the phase-averaged velocity fields. $\tilde{u}_*$ represents the root-mean-square value of the friction velocity at the surface. ΔT is the difference between the surface temperature and the mean temperature within the fluid layer. In the LES, the surface temperature is taken as $T(z_0)$. All results are averages over the surface and the time interval $30 \leqslant t/t_* < 35$

steady state. The plotted heat flux profiles deviate from linear shapes because we average at η = const. and not at z = const. In the DNS we see from figure 10(*e*) that quite large portions of the heat flux stem from the conductive fluxes. The rather smooth profiles of these conductive fluxes in the lower fraction of the layer reveal that this part is resolved to a large extent in spite of the coarse grid. In the LES, we have identified the SGS parts of total kinetic energy and vertical heat flux (figures 11*d* and 11*e*); obviously the SGS parts are small. The mean temperature profiles are very similar in the DNS and LES cases. In all cases we find increasing temperature in the upper part of the mixed layer with positive heat flux, i.e. countergradient heat flux, as explained for the flat-surface case. The observed variations within the set of LES results are generally small in comparison to scatter in data observed in atmospheric measurements, as reported, for example, by Druilhet *et al.* (1983*b*).

In order to show the mean field induced by the surface undulation, we follow the proposals of Hadfield (1988) and Walko *et al.* (1990) and present results which are averaged over time ($30 \leqslant t/t_* < 35$), over the y-direction, and over corresponding positions with respect to the surface phase, so-called 'phase-averages'. For example, figure 12 shows phase-averaged velocity and temperature fields in a vertical plane for case L1514. The basic structure is as to be expected. The fields are strictly periodic with the same wavelength as that of the surface because of the method of averaging. Warm fluid rises from the surface peaks and sinks into surface valleys. The horizontal flow is, as required for continuity, from valleys towards crests. The flow field is not strictly symmetric because of small contributions from circulations which span the whole computational domain. Before applying the code we had made sure that the code guarantees symmetry by testing the results for sets of random initial conditions with corresponding symmetries. Hence, the observed asymmetry reflects the finite set of data from which the averages are evaluated. Larger domain sizes or time periods of averaging would eliminate this asymmetry.

In table 2 we have collected the extreme values of the phase-averaged velocity fields for all the cases. The DNS gives largest extreme values for $\lambda/H = 2$, whereas for LES the largest values occur for $\lambda/H = 4$. For $\lambda/H = 1$, the extreme values grow with amplitude δ, as to be expected. The effect of the domain size (compare cases

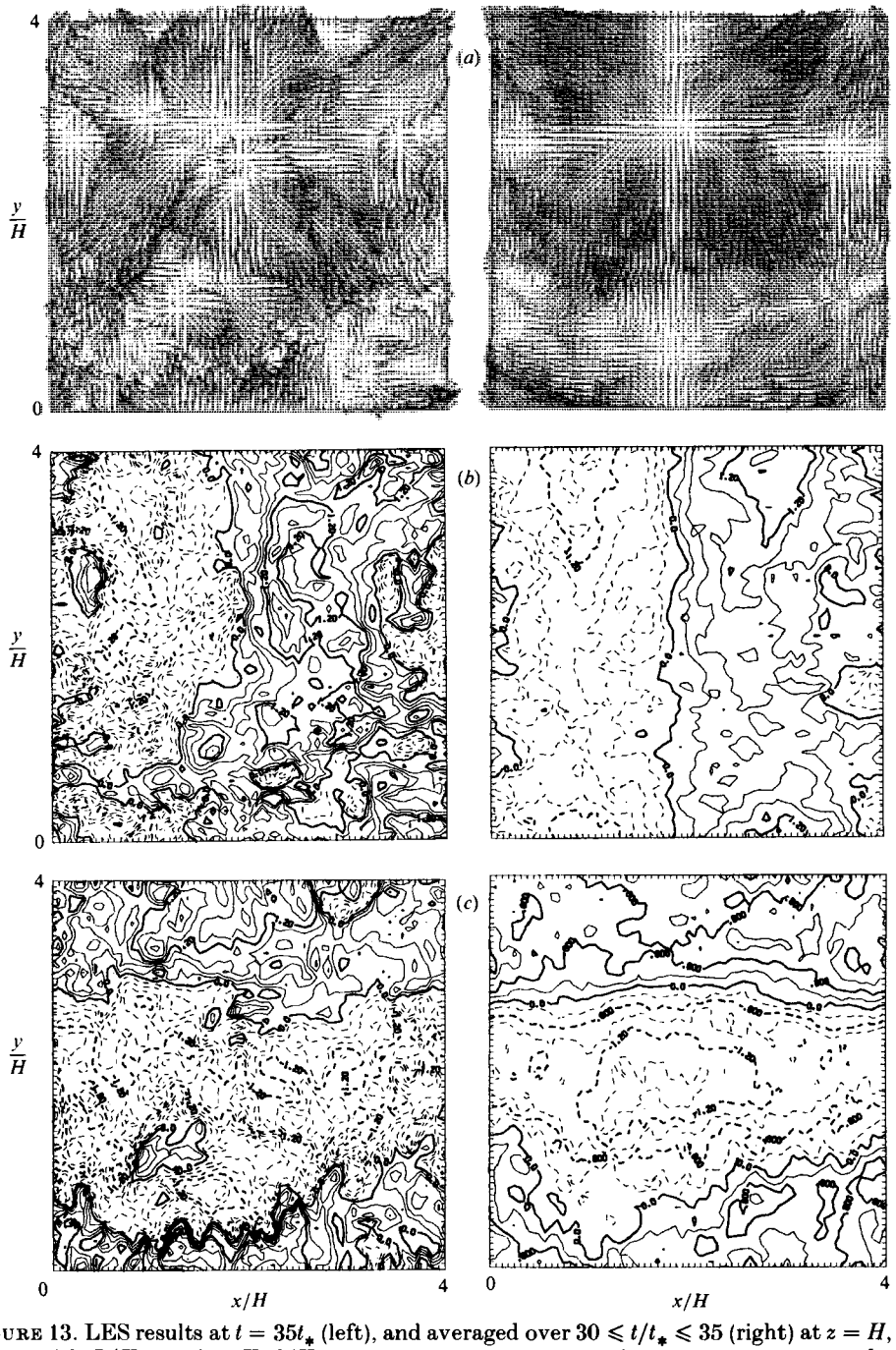

FIGURE 13. LES results at $t = 35t_*$ (left), and averaged over $30 \leqslant t/t_* \leqslant 35$ (right) at $z = H$, for case L1014 with $L/H = 4$, $\lambda = H$, $\delta/H = 0.1$. (*a*) (u, v)-vectors (maximum vector corresponds to, left: $v_{max}/w_* = 2.70$, right: 1.78). (*b*) u-velocity; (*c*) v-velocity: the contour increments are $0.3w_*$, the maximum contour values are $\pm 2.4w_*$ in the left panels and $\pm 1.5w_*$ in the right ones, negative contours are dashed.

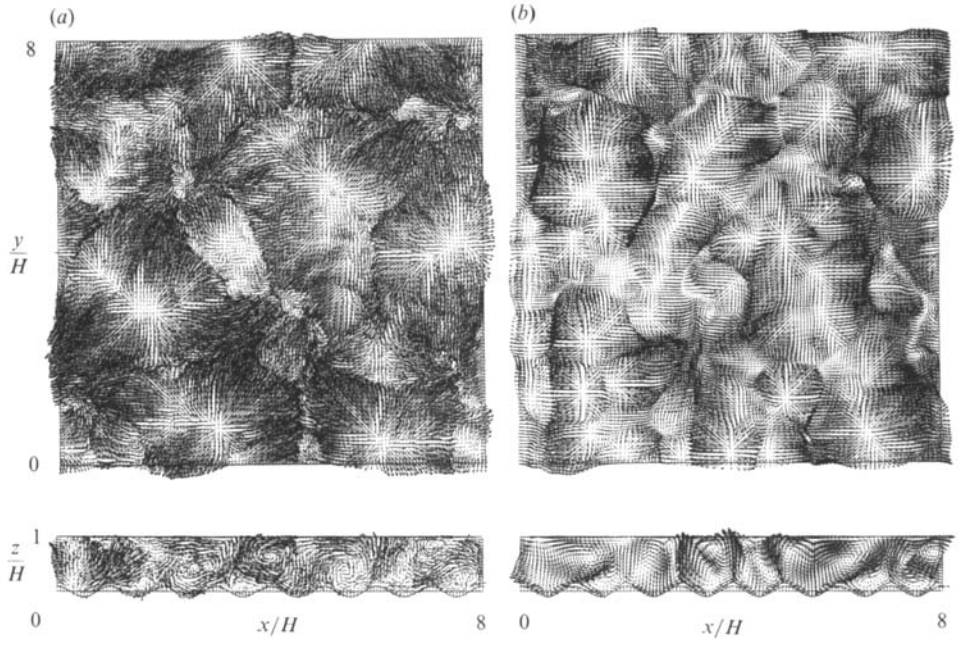

FIGURE 14. Comparison between (*a*) LES and (*b*) DNS in terms of the velocity field at $z = H$ (top) and at $y = 0$ (bottom), averaged from $t/t_* = 30$ to 35 in the case with $L/H = 8$, $\lambda = H$, $\delta/H = 0.1$ (cases D1018 and L1018). Maximum velocities are $1.72w_*$ (DNS) and $1.87w_*$ (LES).

D/L1014 and 1018) is of order 10%. Hence, a domain of size $4H$ is large enough to cover the essential mean properties of the flow.

3.3. *Turbulence structure*

In this section we search for the effects of the wavy lower boundary on the turbulent flow structure. The mean profiles shown in figures 10 and 11 lead us to expect small effects whereas figure 12 suggests considerable contributions from coherent rolls aligned with the surface crests. This section will show, however, that instantaneous flow fields are dominated by random motion components which hide the coherent parts induced by the boundary forcing. In order to make the coherent motion parts better visible, we will present results averaged over a finite time period within the final part of the simulation period where the time-average filters out the short-living small-scale random motions and emphasizes the large-scale and long-living parts of the turbulent motions. For this purpose, we average over the time period $30 \leqslant t/t_* \leqslant 35$. The limits of this interval are arbitrarily selected; the interval length of 5 convective time units is large enough to detect persistent structures but still small enough to show up turbulent motions. If an average were taken over an infinite time period, all motions parallel to the crests of the surface waves would average out because of homogeneity in that direction.

In figure 13, we show the effect of time averaging by comparing instantaneous results to averaged results. This figure applies to case L1014 with $\lambda/H = 1$. We see that the flow fields are quite random in the instantaneous fields. From the velocity vector plot at the top surface, it is hard to identify the direction of the wave crests (which is along the y-coordinate in the vertical). A more regular structure becomes visible, however, in the averaged vector plot and the averaged contour plots.

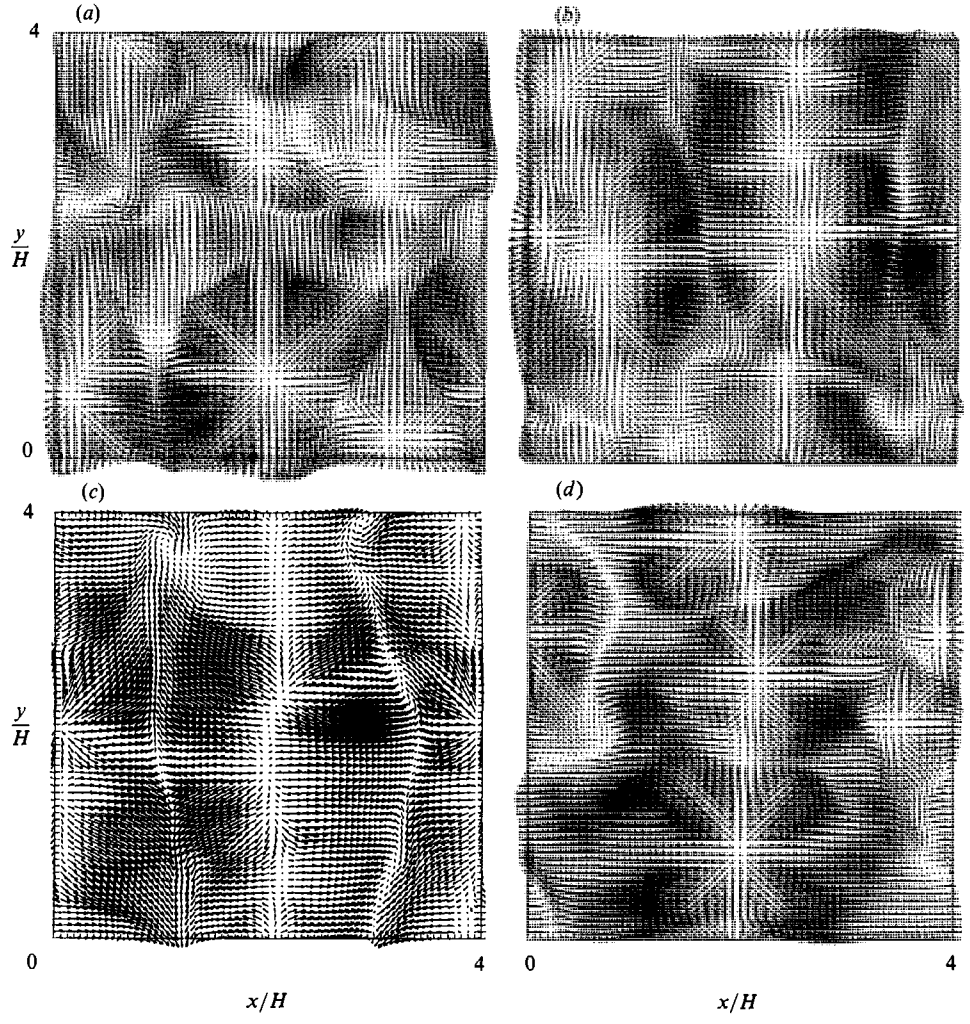

FIGURE 15. Influence of wavelength of orography on the velocity field in the DNS (time averaged from 30 to 35, at $z = H$): (*a*) flat surface, case D00U4; (*b*) $\lambda = H$, case D1014; (*c*) $\lambda = 2H$, case D1024; (*d*) $\lambda = 4H$, case D1044. In the wavy cases, $\delta/H = 0.1$. Maximum velocity vectors in units of w_* are 1.47, 1.77, 1.80, 1.51, respectively.

Obviously, in this case, the flow is predominantly composed of two rolls, a 'primary' one with axis parallel to the wave crests and a 'secondary' one perpendicular to the crests. The roll diameters are, however, four times greater than those one would expect from the wavelength λ. In the time-averaged results the motion amplitudes are roughly 60 to 70% of those in the instantaneous fields. This can be measured in terms of the ratio of maximum velocity vectors (1.78/2.70) or the amplitude of the maximum contour lines. Hence, about half the motion energy is carried by long-living flow structures and this structure is best seen from plots of time-averaged fields.

In figure 14, we show the results from two of our 'largest' (in terms of domain size and computer effort) simulations and compare DNS with LES. The basic structure looks the same in both cases: the flow is dominated by the few strong updraughts that reach the top boundary. They cause the flow to diverge. Several such divergent

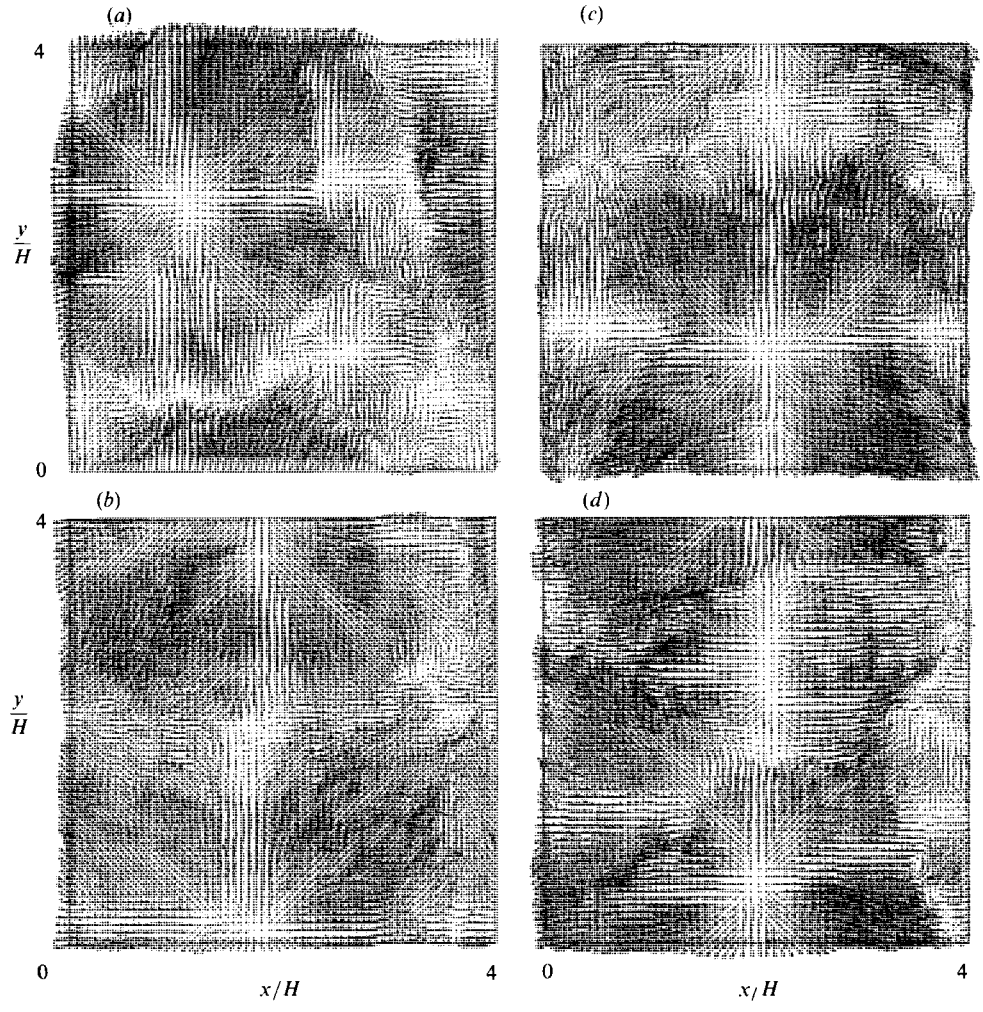

FIGURE 16. As figure 15 but in the LES: (*a*) L00U4; (*b*) L1014; (*c*) L1024; (*d*) L1044. Maximum normalized velocities are 1.69, 1.79, 1.93, 1.91, respectively.

flows collide along lines where the fluid sinks back to the mixed layer. The amplitude of the maximum vector in the DNS is only slightly smaller than in the LES. Hence the flow predicted by DNS for this Reynolds number comes close to the asymptotic state at very large Reynolds number. However, some differences are obvious. As expected, the DNS results look smoother. Also, they show smaller horizontal structures. The characteristic horizontal scale can be estimated to be $2H$ for the DNS but about $3H$ to $4H$ for the LES. The difference in scales is presumably a consequence of differences in horizontal mixing as reflected by the very different horizontal variance profiles which we showed in figures 10(*a*, *b*) and 11(*a*, *b*). The stronger horizontal mixing in the LES causes a reduction of motion components at smaller scales, relatively to those in the DNS. Although these results are obtained for an undulating lower boundary, the results look isotropic and do not show up this forcing. For both simulations, the vertical cross-sections show clearly that the dominant turbulent scales are larger than the wavelength of the surface. It should be noted that the DNS results have been obtained for the same parameters as in

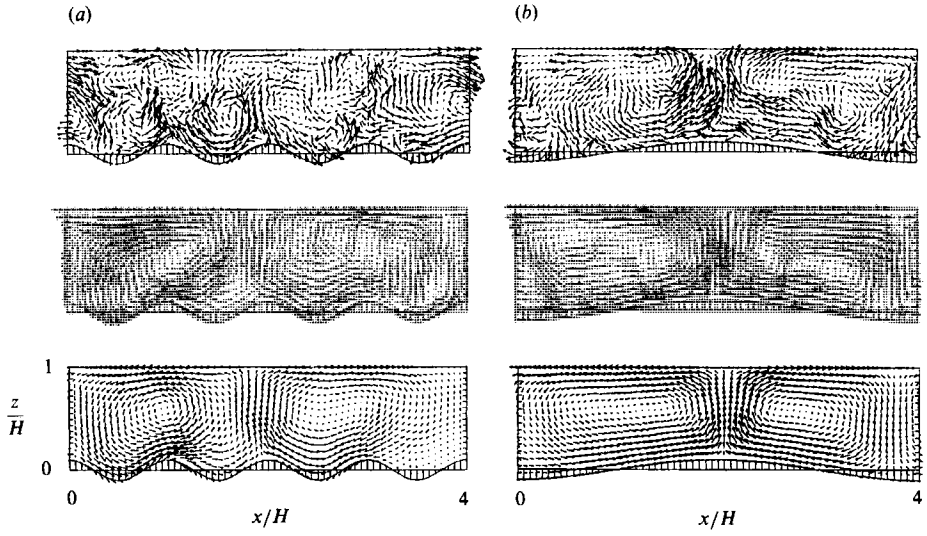

FIGURE 17. Influence of averaging and wavelength of orography on the velocity field in the LES in a vertical plane for various averages and wavelengths. (*a*) $\lambda = H$, case L1014; (*b*) $\lambda = 4H$, case L1044. Top: instantaneous result at $t = 35t_*$. Middle: result averaged from $t/t_* = 30$ to 35. Bottom: Result averaged over the same time interval and in addition over the y-coordinate. Maximum normalized velocity vectors, from top to bottom are, (*a*) 2.20, 1.50, 1.03; (*b*) 2.59, 1.63, 1.34.

Krettenauer & Schumann (1989*b*) except for a larger domain size. Their smaller domain size caused the solutions to show a more regular bimodal cross-roll structure. Obviously, it is important to use a domain size which covers at least the large-scale turbulent motions.

It appears as if short wavelengths excited by the surface are destroyed by the turbulent motions, but larger wavelengths might persist. In figures 15 and 16 we show results from DNS and LES for flat and undulating surfaces with various wavelengths. These figures are selected to identify the effects of surface wavelength on the flow structure at finite and infinite Reynolds numbers (as far as possible by LES). In all cases, the effect of the surface structure on the flow structure is weak. In figure 15(*d*), for $\lambda = 4H$, we observe a flow pattern which indicates several updraughts along the crest of the surface wave. In the corresponding figure 16(*d*), we find that these plumes have merged together to form one updraught along the crest. Such a contiguous updraught is observable in figure 15(*d*), but not in figure 16(*d*), for $\lambda = 2H$. Hence, the DNS seems to have a preference with respect to $\lambda = 2H$, whereas the LES preferably selects $\lambda = 4H$.

In figure 17, we look again at the effect of wavelengths and of averaging on the flow structures in terms of velocity vectors, but in a vertical plane. Whereas the instantaneous flow results (top panels) show little regular structure, coherent structures become obvious in time-averaged (middle panels) and in time- and y-direction-averaged results (lower panels). The results show clearly that a wavelength $\lambda = H$ is too small to match the dominant turbulent scales and, therefore, the undulation has little effect. A wavelength of $\lambda = 4H$, however, seems to be close to the inherent lengthscale of the large turbulent eddies and therefore the surface attains a sort of a resonance with the turbulent motion such that, on average (time and space), the surface controls a considerable part (but not all) of the motion field.

Figure 18 and 19 show comparable vertical cross-sections of flow fields averaged

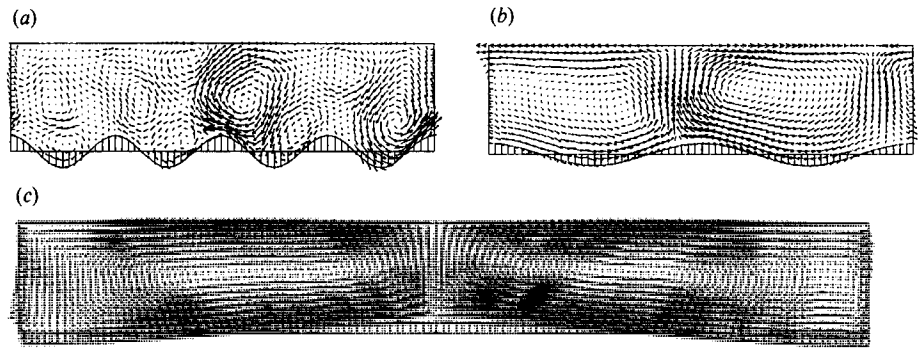

FIGURE 18. Influence of wavelength of orography on the velocity field in the LES in a vertical plane for various surface undulations. These plots represent time- and y-averaged results. (*a*) L1514, (*b*) L1024, (*c*) L1088. Maximum normalized velocity vectors (*a*) 1.32, (*b*) 0.62, (*c*) 1.0.

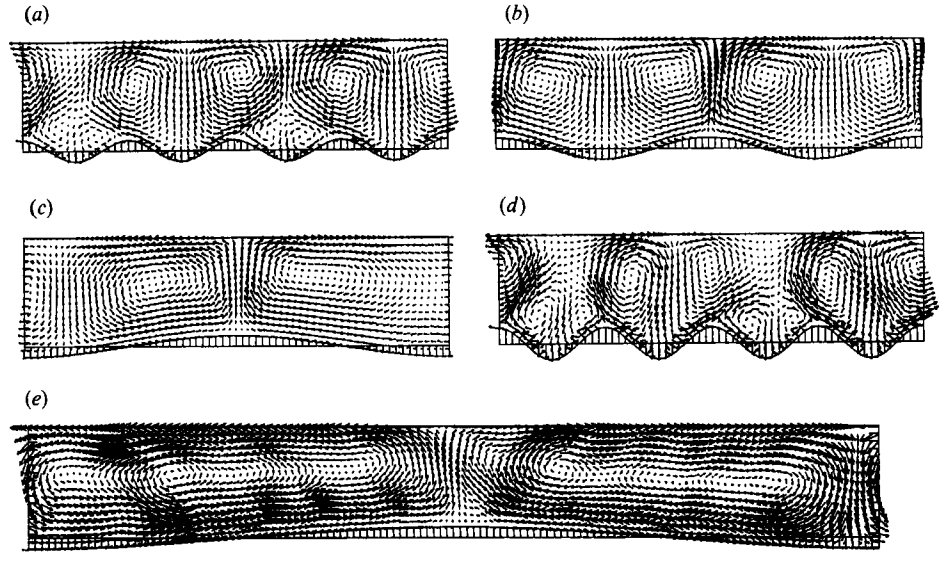

FIGURE 19. As figure 18 but for DNS cases. (*a*) D1014, (*b*) D1024, (*c*) D1044, (*d*) D1514, (*e*) D1088. Maximum normalized velocity vectors (*a*) 1.22, (*b*) 1.32, (*c*) 0.63, (*d*) 1.10, (*e*) 0.60.

over the final five convective time units for all the other simulation cases. We find coherent rolls parallel to the surface waves only for long surface waves. The DNS results for short surface waves show an interesting double vortex structure which is absent in the LES results. Smaller vortices within the valleys interact with the larger scale motions in mixed layers above the crests. To a first approximation, every second valley vortex drives larger vortices above the valley. Such structures may appear rather incidentally in the plots for this particular time interval but, apparently, the stronger turbulent mixing in the LES suppresses such small-scale vortices. These results show that phase-averaged results, as shown in figure 12, are quite misleading with respect to the actual flow structure. The actual structure of the most energetic motions is far from being quasi-two-dimensional.

Up to now, we have discussed the velocity fields: figure 20 shows the temperature field near the lower and upper surfaces for various surface wavelengths. Although these are again time-averaged results, the temperature field still looks very random,

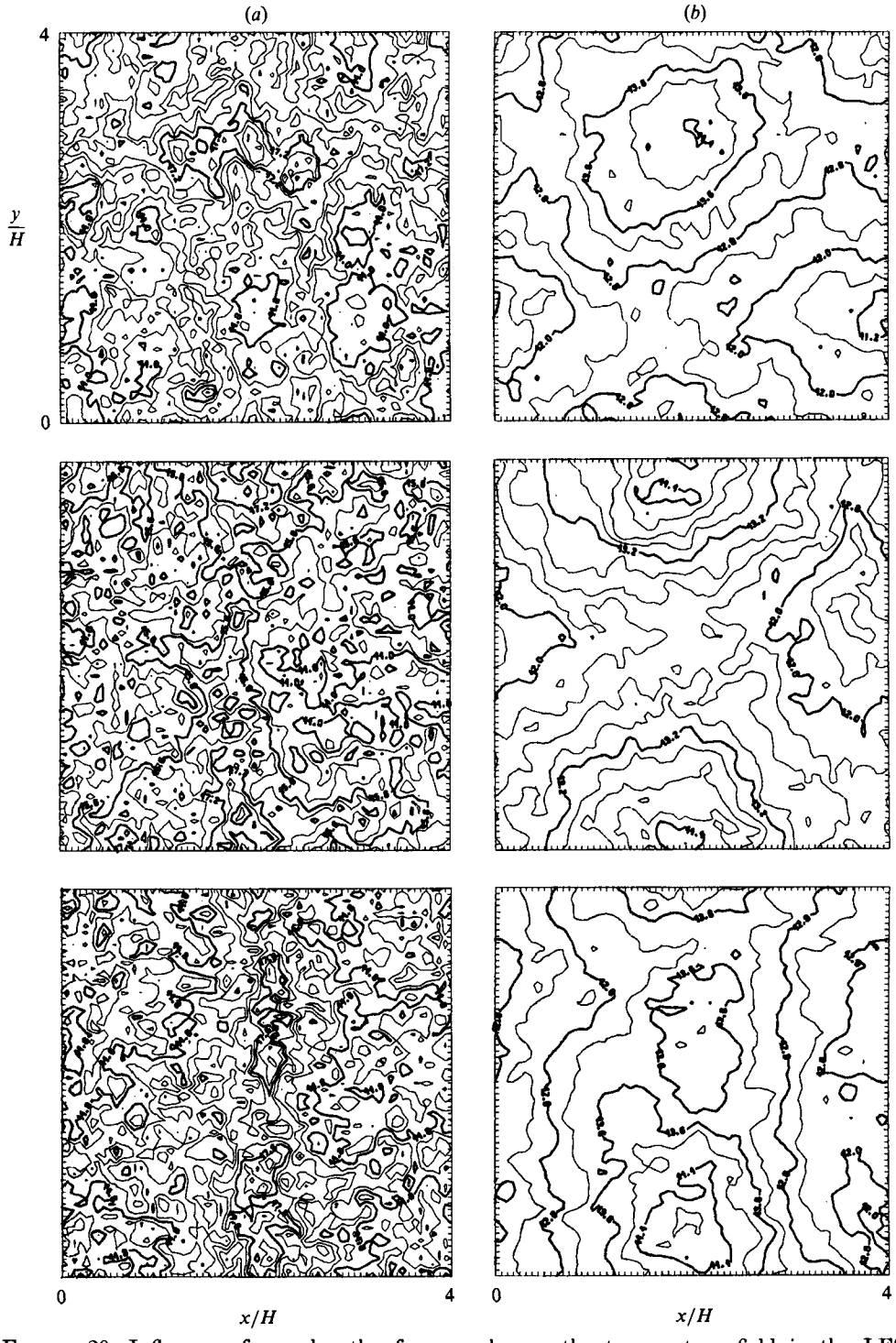

FIGURE 20. Influence of wavelength of orography on the temperature field in the LES for $\lambda/H = 1, 2, 4$ (cases L1014, L1024, L1044) from top to bottom, respectively, time-averaged from $t/t_* = 30$ to 35. (*a*) Temperature at the wavy surface ($\eta = 0.03$); contour increments are $0.8T_*$, $0.8T_*$, $0.7T_*$, from top to bottom, respectively. (*b*) Temperature at the top surface; contour increments are $0.4T_*$, $0.3T_*$, $0.3T_*$, from top to bottom, respectively.

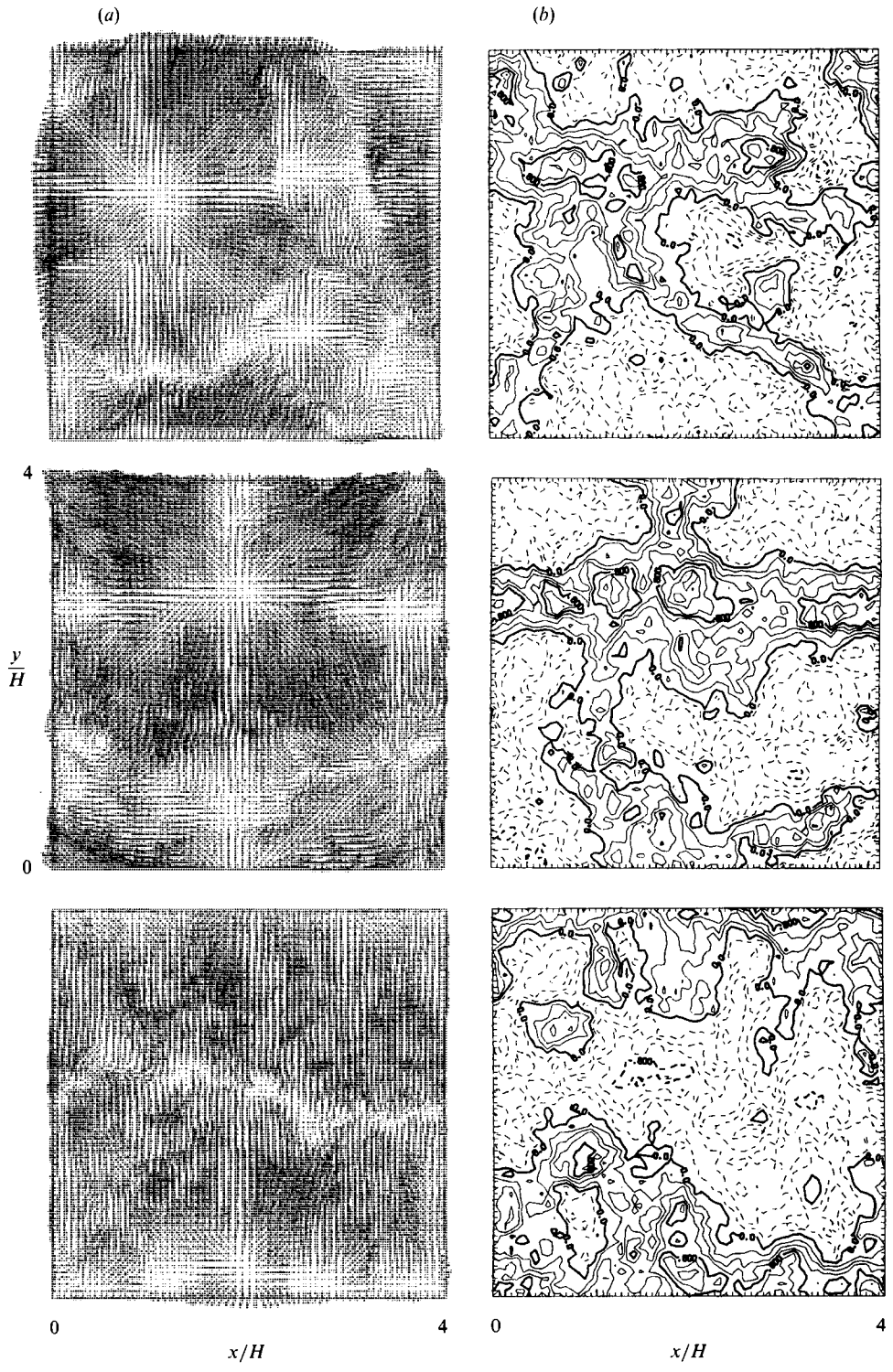

FIGURE 21. Influence of the wave amplitude δ of orography on (*a*) the horizontal velocity vectors (at $z = H$) and on (*b*) the vertical velocity w (at $\eta = 0.5$) in the LES for $\delta/H = 0,0.1, 0.15$ (cases L00U4, L1014, L1514) from top to bottom, respectively, in the time average from $t/t_* = 30$ to 35. Maximum velocity vectors in units of w_*, from top to bottom: 1.89, 1.78, 1.86. Contour increment is $0.2w_*$, dashed contours correspond to negative velocity.

in particular near the lower surface. Only for the maximum wavelength do we see that systematic hot lines form along the surface of the wave crest. A small-scale pattern has to be expected because large-amplitude temperature fluctuations are required in strong correlation with the vertical velocity fluctuations to carry the heat flux which is uniform at the surface. The dominance of small scales is a consequence of the fact that the scale of vertical motions decreases when approaching the surface. In contrast, the temperature at the top surface reveals dominating large-scale motions. For $\lambda = H$, the structure of these motions cannot be classified uniquely. For $\lambda = 2H$, the temperature field is consistent with a cross-roll convection pattern of a primary roll parallel to the wave crests and a secondary roll perpendicular to the crests. This pattern produces maximum temperatures at the positions of updraughts. For $\lambda = 4H$, the pattern is more consistent with one dominant primary roll parallel to the wave crest. Hence, this result shows again the existence of cross-roll motions at $\lambda = 2H$.

In figure 21, we investigate the effects of various wave amplitudes for fixed wavelengths on the flow structure. Here, we plot the velocity field at the upper surface and the vertical velocity component in a horizontal 'plane' at $\eta = 0.5$. The updraughts are organized in polygonal bands. Note that the width of these bands has been increased by the time-averaging procedure. Instantaneous plots are very similar to those reported by Schmidt & Schumann (1989) and Moeng & Rotunno (1990). From the results shown here, we find that even without surface undulation, case L00U4, the largest scales dominate. With undulation, the flow selects rolls, but the axes of these rolls are, as noted above, not parallel but, rather, perpendicular to the waves and these 'secondary' rolls become stronger with increasing wave amplitude. Also the wavelength of the secondary rolls increases slightly with increasing δ, and it approaches $4H$ for case L1514. Overall, this suggests, that short surface waves trigger secondary rolls perpendicular to the crests while long surface waves drive the more expected primary rolls parallel to the surface wave crests. Possible reasons for this effect will be explained in the final section.

3.4. *Lengthscales, spectra and time correlations*

Up to now we have discussed lengthscales and timescales based on the motion pictures. Now, we use correlations and spectra to provide a more quantitative analysis. One should be aware that such statistics provide only limited insight into the structure of coherent motions. Nevertheless, spectra should identify the wavelength of maximum response. From Fourier transforms of the turbulent fluctuations along horizontal lines in the x- or y-direction at fixed vertical coordinate η we compute cospectra $\Phi_{fg}(k)$ between any fluctuating components f and g as a function of horizontal wavenumbers k_x or k_y. The results to be shown represent averages over the free horizontal coordinate and over the time interval $30 \leqslant t/t_* < 35$. For instance, figure 22 shows the power spectra of vertical velocity and temperature fluctuations and their cospectrum, i.e. the spectrum of the vertical heat flux. The spectra are plotted in the form used by Schmidt & Schumann (1989) for the heat flux in the CBL over a plane surface. The continuous shape of the spectra is typical for turbulent flows. From DNS the spectra are a little more peaky (shown in Krettenauer 1991) but the general shape again supports the conclusion that the flow is turbulent for $Re = 100$. The present results are obtained for the LES case with undulating surface, $\lambda = H$, and for both the small computational domain ($L = 4H$) and the large domain ($L = 8H$). The wavelength λ and the wavenumber k are related to each other by $k = 2\pi/\lambda$. The smallest wavenumber depends on the domain size,

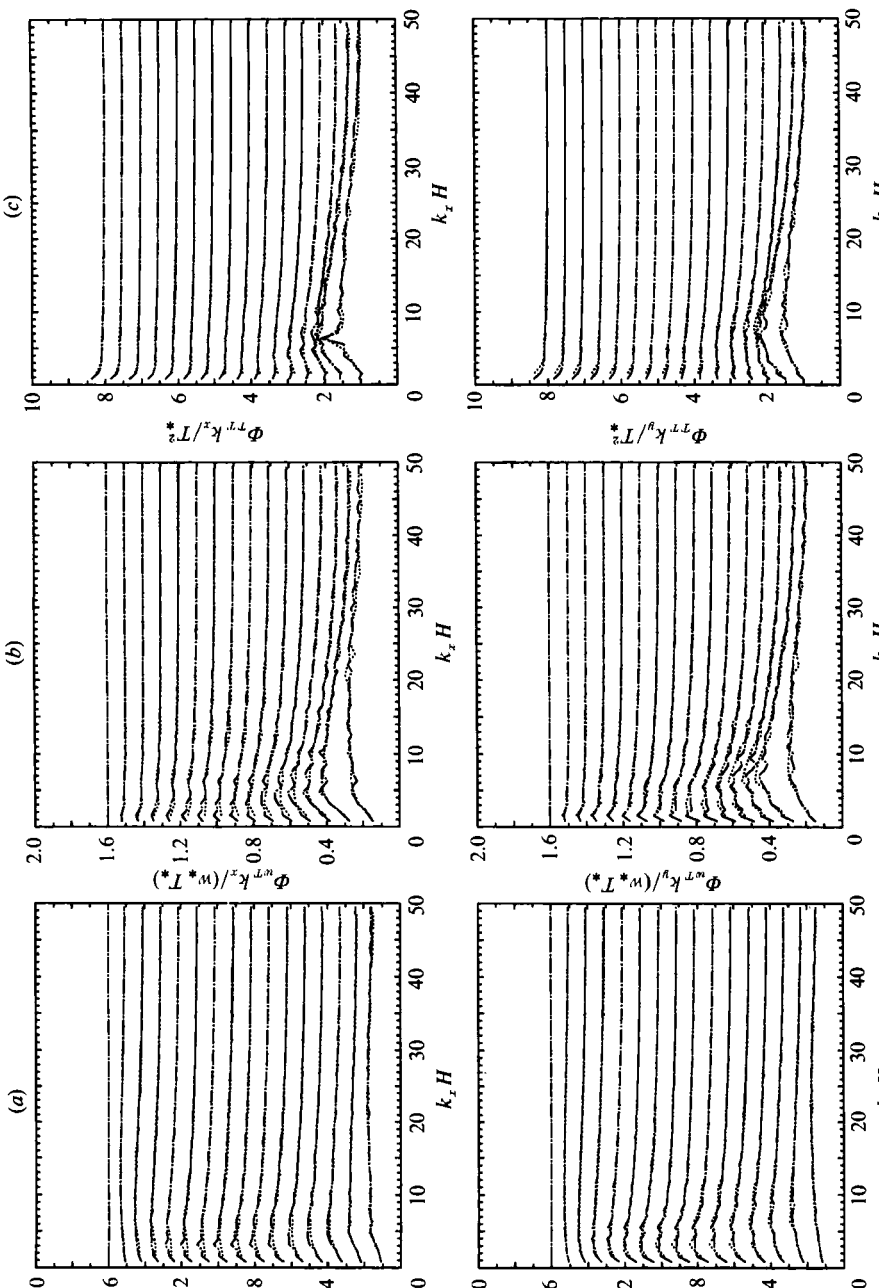

FIGURE 22. (*a*) Power spectra of vertical velocity (*b*), cospectra of heat flux and (*c*) power spectra of temperature fluctuations, versus horizontal wavenumbers k_xH (upper panels) and k_yH (lower panels). The spectra are multiplied by wavenumber. The curves belonging to increasing grid levels are separated by increments of 0.1 (*a*, *b*) or 0.5 (*c*). The lowest curves correspond to the lowest level. —·—, L1018; · · · · ·, L1014.

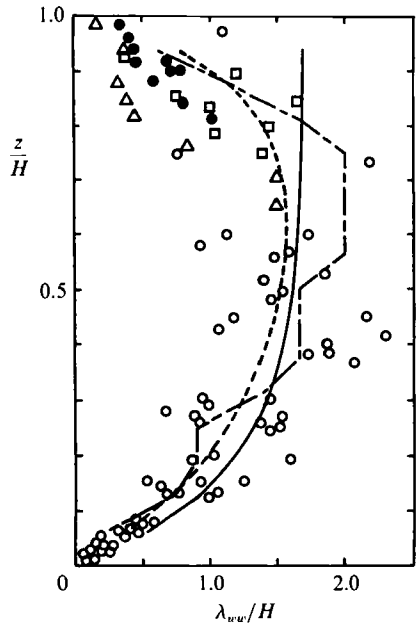

FIGURE 23. Wavelength $\lambda_{ww} = 2\pi/k$ of the spectral maximum of $k\Phi_{ww}(k)$ versus height: –·–·–, Case L00U4 (the result shown is the mean value of those for spectra in the x- and y-directions); symbols, ----, experimental data and fit from Caughey & Palmer (1979); ——, fit from Kaimal *et al.* (1982).

being $k_{\min} H = 0.78$ in case L1018 and 1.57 in case L1014. We observe from figure 22 that the spectra are in close agreement for both cases, i.e. even the largest scales are well approximated in the smaller domain. The surface wavelength $\lambda = H$ corresponds to a non-dimensional wavenumber 6.28 and one would expect that the spectra exhibit peaks of energy at this wavenumber, at least in the x-direction. Most spectra show, however, that this wavenumber is not dominant in the flow. On the contrary, the spectral maxima appear near a wavelength which is smaller than H near the surface but increases to values of the order $4H$ in the upper fluid layer. Only the temperature spectra show a pronounced peak at $k_x H = 6.28$, at least for the lowest grid layer. However, these coherent temperature patterns are only weakly correlated with vertical motions, as we see from the heat flux spectrum in which such a peak is not visible. Since the heat flux at the surface is uniform, such a peak cannot exist. The present results are consistent with the finding of Kaimal *et al.* (1982) who found a rather strong reduction in temperature scales and a weaker increase in vertical velocity scales over uneven terrain.

If the surface modulation enforced two-dimensional roll motions, the x-spectra would be much larger than the y-spectra. This is, however, not the case, as we know already from the motion pictures. Instead, we see that the spectra in both directions have similar amplitudes and shapes and this supports, in a more quantitative manner, our previous finding that the motions are quite isotropic with respect to the vertical axis. The heat-flux spectra near the surface look very similar to the results shown by Schmidt & Schumann (1989). However, in the present case there is no entrainment at the upper boundary and hence the spectra are positive throughout in our case whereas negative flux contributions have been found in the atmospheric boundary layer.

Similar spectra have been computed for all other cases (Krettenauer 1991). Since space does not allow us to show all the details, we follow common practice and

present the wavelengths for which $k\phi_{ww}(k)$ achieves its maximum value. For example, figure 23 shows this wavelength for the case with a plane surface (L00U4) in comparison to results from measurements in atmospheric CBLs. Caughey & Palmer (1979) obtained their data for homogeneous surfaces. Clearly, our numerical result agrees very well with the data, which exhibit considerable scatter. The numerical results even agree with the data in the upper part where the boundary conditions in the atmosphere and in the simulations differ. Obviously, the characteristic wavelength increases from zero near the surface up to order $2H$ in the upper third of the boundary layer and then decreases again to smaller values at the upper boundary. Figure 23 also contains the interpolating curve which Kaimal *et al.* (1982) found to represent measurements over hilly terrain. Their curve indicates somewhat larger wavelengths but the differences appear to be within the scatter of the data.

In figure 24 we report similar lengthscales as obtained from spectra along x- and y-coordinates and from vertical velocity, heat flux and temperature fluctuations. The individual curves are from three cases with different surface wavelengths. It should be noted that the finite domain size $L = 4H$ restricts the possible values of the wavelengths to integer fractions of the domain size. This explains the non-smooth behaviour of these results. (Figure 23 looked smoother because there we had plotted the mean of lengthscales in the x- and y-directions.) As discussed before, long averaging periods are required to give reliable averages, and this is true in particular for integral lengthscales (Lenschow & Stankov 1986) because they are determined by the few large-scale eddies represented in the numerical simulations. Hence, these results bear considerable statistical uncertainty. Nevertheless, we find that there is little systematic variation between the various cases and that the lengthscales in the x- and y-directions are quite close to each other. This is consistent with the findings of Kaimal *et al.* (1982) and it supports in a quantitative manner our previous finding that the surface wave generally has little effect on the mean flow structure. If any systematic trend is present then it consists of an increase in lengthscales in the x-direction with increasing surface wavelength. At the same time, the lengthscales in the y-direction are decreasing, at least partly.

Finally, we evaluate the temporal persistence by means of time correlations, for example, for the horizontal velocity fluctuations,

$$R_u(\Delta t, \eta) = \frac{\overline{u'(t_0)\, u'(t_0 + \Delta t)}}{\overline{u'(t_0)\, u'(t_0)}}, \tag{33}$$

where the averages are taken over the x- and y-directions. This correlation coefficient depends on height η, and time increment Δt. The reference time t_0 is unimportant in the steady state; here, we use $t_0 = 30t_*$. Figure 25(a–c) shows for example the correlation coefficients for $\Delta t = 4t_*$ for two velocity components and for the temperature in various cases. The full curves represent the correlations for the plane surface. We find that the correlation profiles have a shape very similar to the variances themselves. This means, the motion components with largest energy have the largest correlation time. The correlations are quite small, however. Hence, the turbulent motion field changes its shape within a time period of about $4t_*$. A similar result has been obtained by inspection of tracer diffusion by Ebert *et al.* (1989). Considerably larger correlations are, however, found for the cases with surface waves. We observe that the correlation coefficients grow everywhere with increasing surface wavelength. The increase is particularly large with respect to vertical velocity fluctuations near the surface. Figure 25(d) shows the integral time correlation which

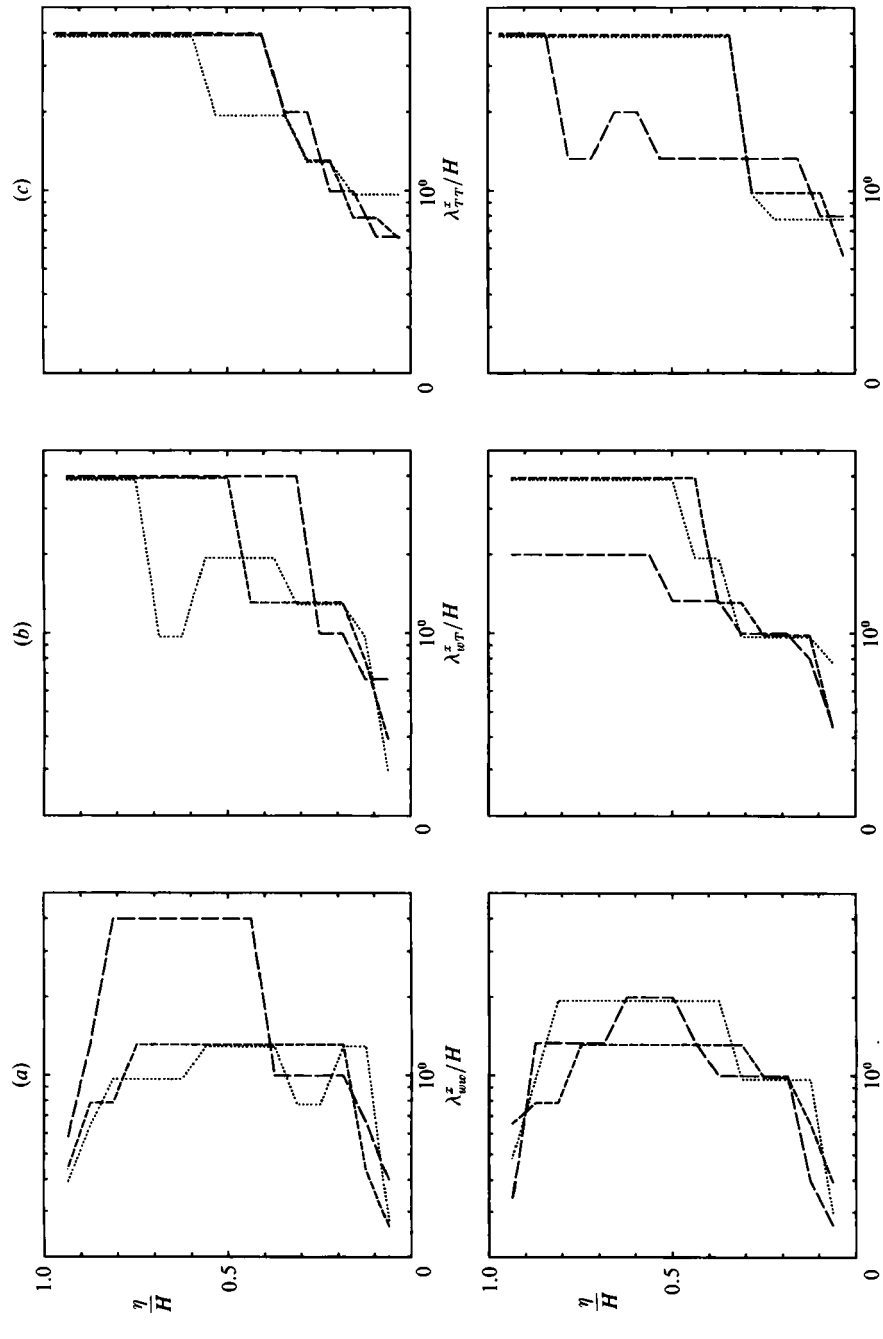

FIGURE 24. Wavelengths of spectral maxima of (*a*) vertical velocity, (*b*) vertical heat flux, and (*c*) temperature fluctuations, along the *x*- and *y*-directions (upper and lower panels) versus vertical coordinate η: ·····, L1014; ----, L1024; ——— L1044. In order to make the curves distinguishable, the results for L1024 have been reduced by 2% while those of L1044 have been increased by the same amount.

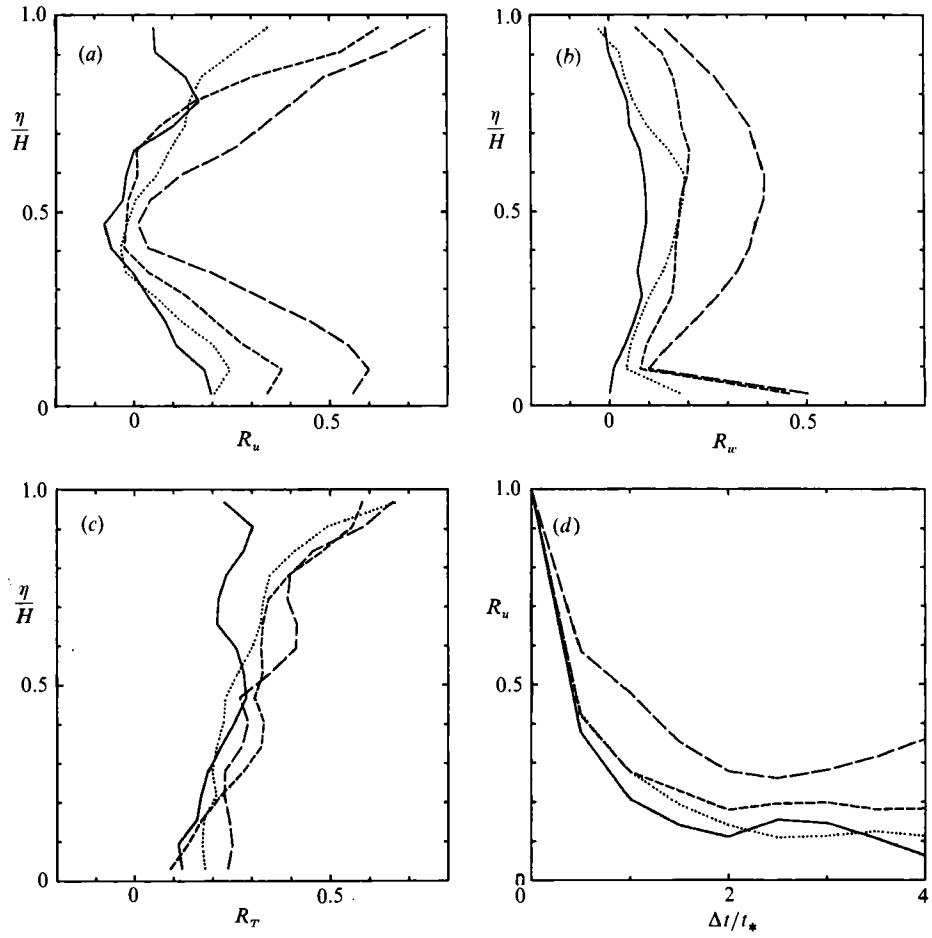

FIGURE 25. Temporal correlations in the LES cases L00U4 (——), L1014 (· · · ·), L1024 (- - - -), L1044 (– – –). (*a*) Correlation between horizontal velocity fluctuations u' at times $t/t_* = 30$ and 34 versus vertical coordinate η, (*b*) as (*a*) but for vertical velocity w', (*c*) as (*a*) but for temperature fluctuations T'. (*d*) Volume-averaged correlation between horizontal velocities u' at times $t = 30t_*$ and $t = 30t_* + \Delta t$ versus time difference Δt.

is computed using averages over all grid points within the computational domain. We see from figure 25 (*d*) that the correlation generally decreases quickly with Δt, but again we find considerably larger correlations in cases with surface waves than over flat surfaces, in particular for $\lambda = 4H$.

3.5. *Heat transfer at the surface*

The temperature difference ΔT between the surface and the bulk of the fluid layer is a measure of heat transfer efficiency. For the rough surface in the LES, the surface temperature is ill-defined and replaced by the value at the height z_0 above the actual (wavy) surface. Note that we have assumed the roughness height to be the same for momentum and for heat transfer. In reality, these parameters may differ considerably if the Monin–Oboukhov relationship is used to determine the effective surface temperature (Beljaars & Holtslag 1991), but this is a minor problem for the present study because the roughness length for heat transfer enters our code only in the diagnostics of the surface temperature. The difference between $T(z_0)$ and the

effective surface temperature is discussed in Schumann (1988). The results for the various cases are listed in table 2. The table also contains the r.m.s. value of the friction velocity as computed for the LES cases. This 'effective' value is of interest because it controls the turbulent transfer processes at the surface (Schumann 1988).

The temperature differences are smaller in the DNS than in the LES cases because of the rather large conductive heat transfer. The surface undulation has very little effect on the heat transfer, and we can hardly find any systematic trend with variations of λ and δ. Obviously the strong (quadratic) influence of the wave amplitude which was found for subcritical convection by Kelly & Pal (1978) does not extend into the turbulent range. The LES results are close to the values found by Schmidt & Schumann (1989) for a CBL with a flat surface. They considered various values of z_0 relative to the boundary-layer depth z_i. For the same value of the roughness height relative to the boundary-layer depth as used in this study, the CBL results are $\tilde{u}_*/w_* = 0.108$, and $\Delta T/T_* = 49.1$ (Schumann 1988; Schmidt & Schumann 1989). The effect of variations in the Reynolds number on the heat transfer over a wavy surface was discussed in Krettenauer & Schumann (1989*b*).

4. Discussion and conclusions

In summary, the comparison between the LES results for a flat surface with the experimental results from Adrian *et al.* (1986) shows that the LES results can be taken to be as reliable as such laboratory measurements for high-Rayleigh-number flows. The DNS results show that the convection is fully turbulent for a Reynolds number $Re = 100$. This was not so clear in the previous study (Krettenauer & Schumann 1989*b*) in which the lateral domain size was $2H$; in that case a more regular bimodal convection pattern developed at this Reynolds number and turbulent structures were obvious only for larger Reynolds numbers. The results of the present study, in particular comparisons of cases with domain size $4H$ and $8H$, indicate that a domain size of $4H$ is about sufficient but also the minimum to cover all important scales. The simulations were run, for reasons of computational effort, with only 16 grid points in the vertical direction and the same grid spacing in the horizontal directions. Evidence from the comparisons with the experimental data of Adrian *et al.* (1986), inspection of SGS contributions, smoothness of profiles, strong decay of spectra at high wavenumbers, and the resolution requirements deduced by Grötzbach (1983) indicate that the resolution is fine enough. The turbulence statistics become approximately steady after about ten convective time units but some statistical uncertainty remains for mean values taken over the finite domain, in particular with respect to characteristics of large-scale motions.

We find that the volume-averaged kinetic energy over wavy surfaces differs only slightly from that over flat surfaces. Figure 11 (*d*) suggests a small increase for large wavelengths. The energy level results from an equilibrium between the buoyant production rate and the viscous dissipation rate ϵ. The mean production rate equals $\frac{1}{2}\beta g Q_S$ for flat as well as for wavy surfaces because the mean heat flux decreases linearly from its surface value Q_S to zero at the top. The dissipation rate $\epsilon = E^{\frac{3}{2}}/L_\epsilon$ might be a little less for large-scale coherent motions with effectively larger dissipation length L_ϵ and therefore the energy may be slightly larger. On the other hand, the coherent motions cause surface friction and internal shear which increase the dissipation rate to cause reduced energy. In any case, the results show that the variations in kinetic energy are small. But the large-scale motions induced by the surface waves cause some increase of velocity variance in the direction of the waves

and consequently a small reduction in vertical and cross-stream variances, in particular for $\lambda > 2H$. An increase of vertical variance is found only for very short surface wavelengths and this might be a nonlinear geometrical effect since the horizontal motions at steep slopes are strongly correlated with vertical components. A simple theoretical model to explain these observations is described in Schumann (1992).

The phase-averaged results, see figure 12 and table 2, show coherent motions with maximum amplitude for a critical wavelength. The existence of a critical wavelength is to be expected. At smaller wavelengths the horizontal mixing tends to destroy vertical motions induced at the scales of the surface wave. At larger wavelengths vertical mixing reduces the amplitude of large-scale horizontal motions. Further, large-scale motions require long times to get established so that such regular structures can hardly develop in atmospheric boundary layers. As shown by Priestley (1962) and Ray (1965), anisotropic turbulence with stronger horizontal than vertical mixing increases the horizontal scale of the convection. At small Reynolds numbers, the mixing is more isotropic because of contributions by the isotropic molecular diffusivity. At high Reynolds numbers, however, horizontal mixing is much more effective than vertical because of much larger horizontal than vertical velocity variance, compare figures 10 (a, c) and 11 (a, c), and because of larger horizontal than vertical scales of the turbulent motions, see figure 24. Hence, the difference between the critical wavelengths in DNS ($\lambda = 2H$) and LES ($\lambda = 4H$) is caused by the difference in horizontal mixing which is much larger in the LES than in the DNS.

The motion structures are persistent over longer time periods in the presence of surface waves which seem to 'lock' the motions to fixed positions. Briggs (1988) observed a similar effect for convection over flat terrain with variable surface heating. The convection pattern is composed of large-scale components induced by the surface wave together with a turbulent convective structure as it arises over flat surfaces. The coherent part is rather small in comparison to the latter, in particular for short surface wavelengths and in the upper part of the mixed layer. This was clearly identified from the motion fields and the spectral analysis. At the top of the domain, for $\lambda = H$, the velocity field is much more isotropic in structure than one might have expected over wavy terrain. The coherent parts are more visible if one averages over a finite time period because such averages filter out the more random motion components. The lengthscale of maximum spectral response over wavy terrain is close to the values over flat terrain. Maximum spectral response is found for the temperature fluctuations near the surface. Intuitively one would expect that the 'primary' rolls with axes parallel to the crests will dominate. However, we find 'secondary' rolls with axes perpendicular to the wave crests at short surface wavelengths. The existence of secondary rolls was indicated by the stability analysis of Pal & Kelly (1979) and the numerical results of Krettenauer & Schumann (1989*b*). As a further explanation we note that primary rolls with wavelengths larger than the surface wave have to pass over the wave crests so that their effective vertical dimension is less than H. Friction at the crests and vertical mixing induced by plumes rising from them tend to damp the primary rolls. In contrast, secondary rolls span on average a thicker layer with less surface friction. Therefore, the circulation intensity in the secondary rolls can become larger than in the primary rolls at short surface wavelengths. This explanation is consistent with the observed increase of motion amplitude of secondary rolls for increasing surface wave amplitude δ. Finally, the secondary rolls are free to select their 'optimum' wavelength in the y-direction

with maximum motion amplitude whereas the primary ones are restrained to the surface wavelength and are therefore less intense. This is corroborated by figure 21 which shows that the secondary rolls become more pronounced for steep surface waves and select the apparently optimal wavelength of about $4H$.

Unfortunately, laboratory data are not available for turbulent convection over wavy surfaces. However, our results agree approximately with field observations over more irregular terrain (Kaimal *et al.* 1982; Druilhet *et al.* 1983*b*; Jochum 1988; Huynh *et al.* 1990) which reveal little differences with respect to observations over homogeneous surfaces. The weak increase in lengthscales for vertical velocity but stronger reduction of such scales for temperature fluctuations over wavy terrain as found by Kaimal *et al.* (1982) agrees qualitatively with what we found from the spectral analysis.

Walko *et al.* (1990) reported results for a CBL (with a rather weak inversion above the mixed layer) for convection over a sinusoidal surface with $\delta/H = 0.15$, and two values of the wavelength, $\lambda/H = 1$ and 2. Their results agree with ours in that they also find little difference between the mean profiles for hilly and flat cases. However, they show time- and y-averaged flow fields which are more strongly affected by the surface waves than we found in the corresponding figure 18(*a*). It might be possible that this difference comes from the different top boundary condition. The rigid lid deflects upward motions from thermals into horizontal components by pressure forces more effectively than any weaker inversion layer. It also appears plausible that these stronger horizontal motions have larger wavelengths. Hence, the sensitivity of the flow structure to surface forcing will depend, at least slightly, on the inversion strength. In principle, the present method could easily be applied to cases with a free stable troposphere above the mixed layer. However, then the results depend also on the stability of the stratification at and above the inversion so that a single case study would not be conclusive.

In summary, we have investigated the structure of the convective layer above wavy terrain. We have identified some rather surprising effects of the two-dimensional terrain on three-dimensional motions. In particular we find a kind of 'resonant' response of turbulence to surface undulation at wavelengths which equal the inherent scale of the convective circulation over homogeneous surfaces. Two-dimensional mean fields hide the complex nature of the most energetic motion structure. Three-dimensional motions are enforced by terrain, like rolls perpendicular to the wave crests, which cannot be predicted with two-dimensional models. On the other hand, the results show that wavy terrain has rather small effects on the mean turbulence profiles and the heat exchange at the surface, at least for zero mean wind and surface waves with $\delta \leqslant 0.15$, $1 \leqslant \lambda/H \leqslant 8$, studied in this paper. In view of the fact that the maximum surface slope reaches 43° in one of the cases, this is a noteworthy result. For more realistic comparisons with atmospheric cases, this study should in the future be extended to include more irregular terrain and a non-zero mean wind.

This work was supported by the Deutsche Forschungsgemeinschaft.

REFERENCES

Adrian, R. J., Ferreira, R. T. D. S. & Boberg, T. 1986 Turbulent thermal convection in wide horizontal fluid layers. *Expts. in Fluids* **4**, 121–141.

Beljaars, A. C. M. & Holtslag, A. A. M. 1991 Flux parameterization over land surfaces for atmospheric models. *J. Appl. Met.* **30**, 327–341.

BRIGGS, G. A. 1988 Surface inhomogeneity effects on convective diffusion. *Boundary-Layer Met.* **45**, 117–135.

BUSSE, F. H. 1978 Non-linear properties of thermal convection. *Rep. Prog. Phys.* **41**, 1930–1967.

CAUGHEY, S. J. & PALMER, S. G. 1979 Some aspects of the turbulent structure through the depth of the convective boundary layer. *Q. J. R. Met. Soc.* **105**, 811–827.

CLARK, T. 1977 A small-scale dynamical model using a terrain-following coordinate transformation. *J. Comput. Phys.* **24**, 186–215.

DEARDORFF, J. W. 1970 Convective velocity and temperature scales for the unstable planetary boundary layer and for Rayleigh convection. *J. Atmos. Sci.* **27**, 1211–1213.

DRUILHET, A., FRANGI, J. P., GUEDALIA, D. & FONTAN, J. 1983*a* Experimental studies of the turbulence structure parameters of the convective boundary layer. *J. Clim. Appl. Met.* **22**, 594–608.

DRUILHET, A., NOILHAN, J., BENECH, B., DUBOSCLARD, G., GUEDALIA, D. & FRANGI, J. 1983*b* Étude expérimentale de la couche limite au-dessus d'un relief modéré proche d'une chaîne de montagne. *Boundary-Layer Met.* **25**, 3–16.

EBERT, E. E., SCHUMANN, U. & STULL, R. B. 1989 Nonlocal turbulent mixing in the convective boundary layer evaluated from large-eddy simulation. *J. Atmos. Sci.* **46**, 2178–2207.

FIEDLER, B. H. 1989 Scale selection in nonlinear thermal convection between poorly conducting boundaries. *Geophys. Astrophys. Fluid Dyn.* **46**, 191–201.

GARRATT, J. R., PIELKE, R. A., MILLER, W. F. & LEE, T. J. 1990 Mesoscale model response to random, surface based perturbations – a sea-breeze experiment. *Boundary-Layer Met.* **52**, 313–334.

GRAF, J. & SCHUMANN, U. 1991 Simulation der konvektiven Grenzschicht im Vergleich mit Flugzeugmessungen beim LOTREX-Experiment. *Met. Rdsch.* **43**, 140–148.

GRÖTZBACH, G. 1983 Spatial resolution requirements for direct numerical simulation of the Rayleigh–Bénard convection. *J. Comput. Phys.* **49**, 241–264.

HADFIELD, M. G. 1988 The response of the atmospheric convective boundary layer to surface inhomogeneities. *Colorado State University, Atmospheric Science Paper* 433.

HECHTEL, L. M., MOENG, C.-H. & STULL, R. B. 1990 The effects of nonhomogeneous surface fluxes on the convective boundary layer: A case study using large-eddy simulation. *J. Atmos. Sci.* **47**, 1721–1741.

HUYNH, B. P., COULMAN, C. E. & TURNER, T. R. 1990 Some turbulence characteristics of convectively mixed layers over rugged and homogeneous terrain. *Boundary-Layer Met.* **51**, 229–254.

JOCHUM, A. 1988 Turbulent transport in the convective boundary layer over complex terrain. In *Proc. Eighth Symp. on Turbulence and Diffusion, San Diego*, pp. 417–420. Am. Met. Soc.

KAIMAL, J. C., EVERSOLE, R. A., LENSCHOW, D. H., STANKOV, B. B., KAHN, P. H. & BUSINGER, J. A. 1982 Spectral characteristics of the convective boundary layer over uneven terrain. *J. Atmos. Sci.* **39**, 1098–1114.

KELLY, R. E. & PAL, D. 1978 Thermal convection with spatially periodic boundary conditions: resonant wavelength excitation. *J. Fluid Mech.* **86**, 433-456.

KRETTENAUER, K. 1991 Numerische Simulation turbulenter Konvektion über gewellten Flächen. Dissertation; *rep.* DLR-FB 91-12, DLR Oberpfaffenhofen, 162 pp.

KRETTENAUER, K. & SCHUMANN, U. 1989*a* Struktur der konvektiven Grenzschicht bei verschiedenen thermischen Randbedingungen. *Ann. Met.* **26**, 278–279.

KRETTENAUER, K. & SCHUMANN, U. 1989*b* Direct numerical simulation of thermal convection over a wavy surface. *Met. Atmos. Phys.* **41**, 165–179.

LENSCHOW, D. H. & STANKOV, B . B. 1986 Length scales in the convective boundary layer. *J. Atmos. Sci.* **43**, 1198–1209.

MASON, P. J. 1989 Large eddy simulation of the convective atmospheric boundary layer. *J. Atmos. Sci.* **46**, 1492–1516.

MOENG, C.-H. & ROTUNNO, R. 1990 Vertical-velocity skewness in the buoyancy-driven boundary layer. *J. Atmos. Sci.* **47**, 1149–1162.

MOENG, C.-H. & WYNGAARD, J. C. 1989 Evaluation of turbulent and dissipation closures in second-order modeling. *J. Atmos. Sci.* **46**, 2311–2330.

NIEUWSTADT, F. T. M. 1990 Direct and large-eddy simulation of free convection. In *Proc. 9th Intl Heat Transfer Conf., Jerusalem, 19–24 August 1990*, vol. 1, pp. 37–47. ASME.

NIEUWSTADT, F. T. M., MASON, P. J., MOENG, C.-H. & SCHUMANN, U. 1991 Large-eddy simulation of the convective boundary layer: A comparison of four computer codes. In *Proc. 8th Turbulent Shear Flow Symp., Munich, 9–11 Sept. 1991, Paper* 1.4.1, 6 pp.

PAL, D. & KELLY, R. E. 1979 Three-dimensional thermal convection produced by two-dimensional thermal forcing. *ASME Paper* 79-HT-109, 8 pp.

PIELKE, R. A. 1984 *Mesoscale Meteorological Modeling*. Academic, 612 pp.

PRIESTLEY, C. H. B. 1962 The width-height ratio of large convective cells. *Tellus* **14**, 123–124.

RAY, D. 1965 Cellular convection with nonisotropic eddys. *Tellus* **17**, 434–439.

SCHÄDLER, G. 1990 Triggering of atmospheric circulations by moisture inhomogeneities of the earth's surface. *Boundary-Layer Met.* **51**, 1–29.

SCHMIDT, H. 1988 Grobstruktur-Simulation konvektiver Grenzschichten. Thesis, University of Munich; *Rep.* DFVLR-FB 88-30, DLR Oberpfaffenhofen, 143 pp.

SCHMIDT, H. & SCHUMANN, U. 1989 Coherent structure of the convective boundary layer deduced from large-eddy simulation. *J. Fluid Mech.* **200**, 511–562.

SCHUMANN, U. 1988 Minimum friction velocity and heat transfer in the rough surface layer of a convective boundary layer. *Boundary-Layer Met.* **44**, 311–326.

SCHUMANN, U. 1989 Large-eddy simulation of turbulent diffusion with chemical reactions in the convective boundary layer. *Atmos. Environ.* **23**, 1713–1727.

SCHUMANN, U. 1990 Large-eddy simulation of the upslope boundary layer. *Q. J. R. Met. Soc.* **116**, 637–670.

SCHUMANN, U. 1991 Subgrid length-scales for large-eddy simulation of stratified turbulence. *Theoret. Comput. Fluid Dyn.* **2**, 279–290.

SCHUMANN, U. 1992 A simple model of the convective boundary layer over wavy terrain with variable heat flux. *Beitr. Phys. Atmos.* **64**, No. 3 (in press).

SCHUMANN, U., HAUF, T., HÖLLER, H., SCHMIDT, H. & VOLKERT, H. 1987 A mesoscale model for the simulation of turbulence, clouds and flow over mountains: Formulation and validation examples. *Beitr. Phys. Atmos.* **60**, 413–446.

SCHUMANN, U. & SWEET, R. A. 1988 Fast Fourier transforms for direct solution of Poisson's equation with staggered boundary conditions. *J. Comput. Phys.* **75**, 123–137.

SCHUMANN, U. & VOLKERT, H. 1984 Three-dimensional mass- and momentum-consistent Helmholtz-equation in terrain-following coordinates. In *Notes on Numerical Fluid Mechanics*, vol. 10 (ed. W. Hackbusch), pp. 109–131. Vieweg.

SMOLARKIEWICZ, P. K. 1984 A fully multidimensional positive definite advection transport algorithm with small implicit diffusion. *J. Comput. Phys.* **54**, 325–362.

SORBJAN, Z. 1990 Similarity scales and universal profiles of statistical moments in the convective boundary layer. *J. Appl. Met.* **29**, 762–775.

STULL, R. B. 1988 *An Introduction to Boundary Layer Meteorology*. Kluwer, 664 pp.

SYKES, R. I. & HENN, D. S. 1989 Large-eddy simulation of turbulent sheared convection. *J. Atmos. Sci.* **46**, 1106–1118.

WALKO, R. L., COTTON, W. R. & PIELKE, R. A. 1990 Large eddy simulation of the CBL over hilly terrain. In *Proc. 9th Symp. on Turbulence and Diffusion, Roskilde, Denmark, April 30–May 3*, pp. 409–412. Am. Met. Soc.

WILCZAK, J. M. & PHILLIPS, M. S. 1986 An indirect estimation of convective boundary layer structure for use in pollution dispersion models. *J. Clim. Appl. Met.* **25**, 1609–1624.